POLITECNICO DI TORINO

Corso di Laurea Magistrale in
NANOTECHNOLOGIES FOR ICTs

Tesi di Laurea Magistrale

Mechanical dynamics of graphene layers

Relatore:
Prof. Carlo Ricciardi

Correlatore:
Dott. Stefano Stassi

Candidato:
Federico Fantolino

A.A. 2017/2018

Acknowledgement

First of all, I would like to thank my Supervisor Prof. Carlo Ricciardi, who helps, supports and he has stimulated me in my research. Secondly, I want to thank Dr. Stefano Stassi, who was the most important guide along the whole thesis path.
I thank my parents, Valter Fantolino and Mariarosa Squizzato, for having endured me during these years and for their financial commitment, i will never be able to thank them enough. A special thanks to my brother Edoardo and my cousin Francesca who during these years have managed to endure all my difficulties, transmitting me always happiness. A special thanks also to the person who changed my life, Giulia, who was able to transform me into a better person, always accepting all my difficulties.

Federico Fantolino

Summary

Graphene is the thinner material that exists in nature and it is an allotropic carbon state. Its shape, resistance and stability can be used to create devices never seen before, causing a scientific revolution. It can be used as ultralow mass detection and ultrasensitive force detection and it is so suitable also in biological and chemical detection. It shows very interesting electrical and mechanical properties. It has a very high electrical conductivity, the electron velocity reaches value of 1/300 the light velocity near the so called Dirac points and it has a high mechanical strength, resistance to breakage and very low mass density that permits it to vibrate at MHz.
Nowadays, due to its peculiar properties, it is one of the most studied material in the research of NEMS. Although graphene has been postulated decades ago, its properties were still unknown. Today it is possible to study them thanks to a new experimental approach discovered by two scientists from Manchester, Dr. Andre Geim and Dr. Kostantin Novoselov, who won the Nobel Prize thanks to it. This allowed to obtain the free standing single layer graphene for the first time.

In this thesis the mechanical properties of graphene are studied, by manufacturing what are so called Graphene Drums. These were fabricated and produced at Chilab and Politecnico di Torino laboratories. First of all the graphene is produced by the Chemical Vapor Deposition CVD over a Copper foil by using the NanoCVD, which permits to obtain a large graphene layer.
Subsequently it proceeds with the fabrication and the design of the substrate by using Silicon dioxide SiO_2, this is why graphene sticks itself very strongly. The design corresponds to dig holes with a diameter that varies between 5 μm and 50 μm with a depth of about 1 μm. In order to reproduce this design, a lithographic process is carried out, where the following wet etching of the SiO_2 is made by using the BOE 6:1.

The transfer can be performed via Wet transfer or Dry transfer.
In the Wet transfer, first of all the the Spin-Coating of PMMA is performed over Cu/-graphene. Subsequently, the etching of Cu is carried out by using ferric chloride $FeCl_3$. Due to the large presence of contaminants and impurities, the PMMA/graphene sheet must perform two baths in demineralized water. The PMMA/graphene sheet is then transferred directly onto the designed substrate, fishing the PMMA/graphene foil from the baker. The last step corresponds to the etching of the PMMA, which can be performed via Wet approach by using Acetone or via Dry making evaporate it into a furnace.
Dry transfer is a process which is very similar to the previous one. The main difference consists in using PDMS as a support for the transfer. The PDMS is latched to the sheet of PMMA/graphene/Cu. Subsequently this permits to press the PDMS/PMMA/graphene

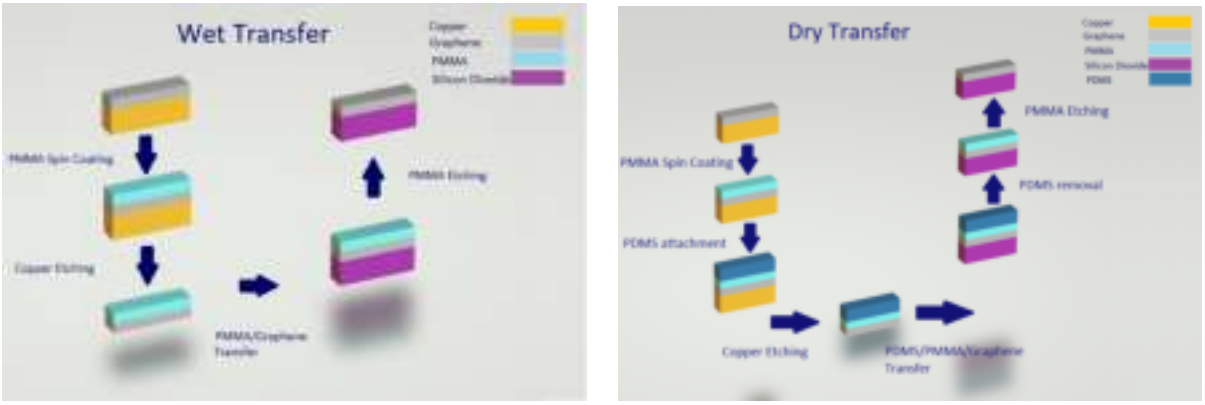

Figure 1: Graphene Wet and Dry transfer

sheet directly on the substrate and firmly anchoring the sheet thanks to a step in temperature.
Several samples were produced by using Wet and Dry transfer. In both cases, the samples are dirty and with a small number of covered holes. The impurities present on the sample are due to the not correct etching of the Cu and PMMA. The turning point corresponds to the removal of the PMMA via Dry etching. This allows to obtain samples which have a high number of covered holes, even if they are still not perfectly intact. Another encountered problem corresponds to the oxidation of Cu foil, in fact, it was possible to note how after a few days the Cu/graphene sheet is oxidized. This does not allow a perfect etching of Cu. A good quality sample is obtained by using fresh Cu/graphene sheet.

The characterization of the samples is carried out by using the Vibrometer in "White Light Mode" and the Scanning electron microscope SEM. These two techniques permit to verify the effective presence of covered holes. In addition, Raman spectroscopy is used to verify the presence of graphene over the holes.

The vibration amplitude of the membranes is studied by using the Vibrometer, which allows to obtain a Magnitude vs frequency spectrum, which permits to study the mode frequency behavior of the various membranes but also the Q factor and the tension level. This study of modes and Q factor is performed by using Origin, a Non linear fit is performed on the peaks of the various modes. The frequency of the mode corresponds to the maximum abscissa, while in order to obtain the correct Q factor the Non linear fit is made after having square elevated the magnitude of the signal. The Q factor is then obtained $Q = x_c/w$ where x_c corresponds to the maximum abscissa and the w corresponds to the FWHM.
Due to the large number of membranes measured in EPFL and G205n samples, it was possible to analyze the average behavior of the first vibrational mode and the average behavior of the Q factor referred to it. As predicted by the theory, both samples have a trend of the first average frequency mode which is proportional to 1/R where R is the radius of the membrane. Using the average tension level per sample that corresponds to $\sigma_{EPFL} = 0.005[N/m]$ for the EPFL sample and $\sigma_{G205n} = 0.003[N/m]$, it was possible to obtain the best fit of the data obtained.

The two samples show very similar behaviors and their average tension level is of the same order of magnitude. Whereas the average Q factor for both samples does not follow a particular trend, the Q factor values reduces as the diameter decreases. This is strictly linked to the quality of the measurement obtained by the Vibrometer which

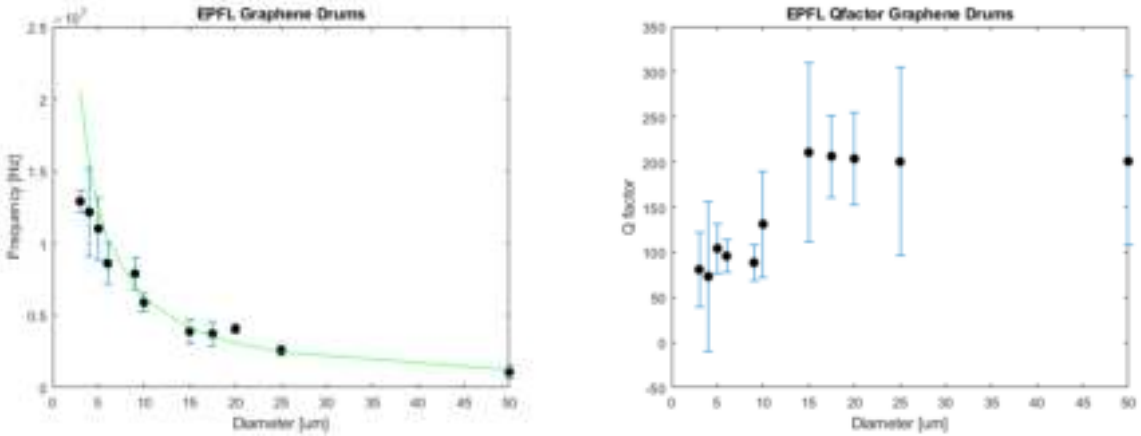

Figure 2: Average first mode frequency with standard deviation vs diameter and Average first mode Qfactor with standard deviation vs diameter of the EPFL sample

results difficult on membranes that have a short diameter and also due to the difficulty of performing the Non linear fit.
This type of average analysis is performed on the first frequency mode because one can note how the subsequent vibrational modes show the phenomenon of modes splitting, which is linked to the presence of breakages and cracks on the membranes.

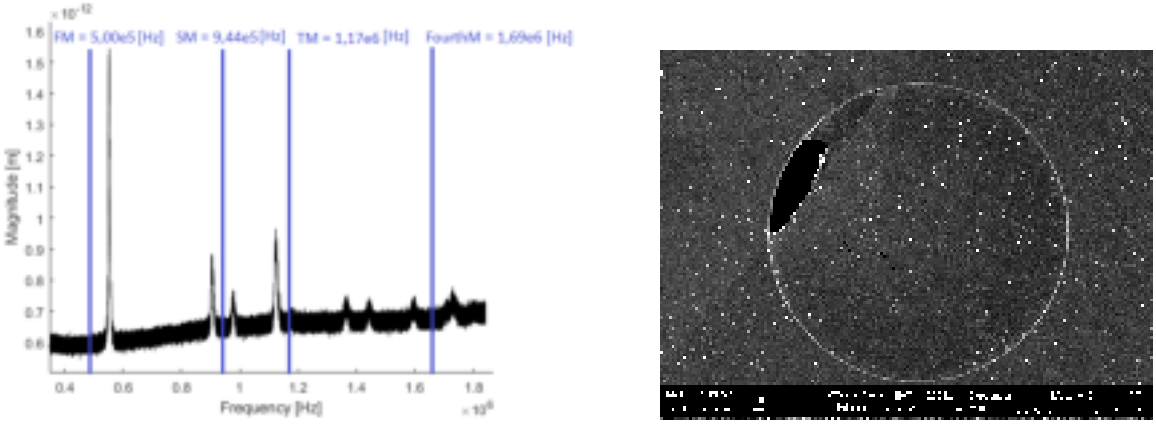

Figure 3: Frequency spectrum of B1A4 membrane, the blue lines corresponds to the position of the simulation values of the first four modes

The splitting is studied and simulated by using Comsol. The results obtained from the simulation reflect the experimental measurement. Intact membranes respect the theoretical behavior, while broken membranes follow the splitting of the modes. The exploitation of the splitting of the vibrational modes can be used as a qualitative analysis of the membrane status just by looking at the frequency spectrum, without using time expending techniques as the Vibrometer in "White Light Mode" or the Scanning electron microscope SEM.

Contents

Introduction

In this thesis the mechanical behavior of graphene layers is examined. Nowadays graphene is a 2D material of great interest due to its remarkable electrical and mechanical properties and it shows a very high electrical conductivity and a high mechanical strength. Although graphene has been postulated many decades ago, its properties were still unknown, this is due to the fact that it was difficult to get a free standing graphene sheets. With the new method discovered by two Manchester scientists Dr. Andre Geim and Dr. Kostantin Novoselov, thanks to which they won the Nobel price, the properties of graphene could be studied and understood. In this thesis, in fact, after a brief introduction on the crystallographic structure of graphene and its main electrical and mechanical properties, which are described in the first chapter, it moves on to the description of how the mechanical properties of graphene have been studied. The following chapter treats the whole theory regarding two dimensional bending vibration of plates and membranes. It starts to describe the ideal behavior of the plates, where stress is not presented, and then it arrives at the most complete description of the stressed circular membrane. This theoretical treatment is fundamental, because in this work, in order to study the mechanical properties of graphene, Graphene Drums were designed and fabricated . These devices were fabricated in the Chilab and Politecnico di Torino laboratories. The manufacturing process is described in details in the Experimental chapter. The silicon substrate for the graphene drums were designed and developed to optimize the transfer graphene process. It consists in holes of different diameters, in order to obtain a large number of graphene membranes with different sizes. The graphene used in this work were produced with a process called Chemical Vapor Deposition (CVD). Successively, the graphene deposited on copper substrate were transferred on the silicon pattern substrate, which represents the most difficult and important step. For this purpose, two different transfer approaches were carried out, Wet-transfer and Dry-transfer. Subsequently, all the measurement techniques used to accurately characterize the samples produced are adequately described. The Laser Doppler Vibrometer was used for the vibrational measurements of the graphene drums, while the Scanning Electron Microscope (SEM), the Vibrometer in "White Light Mode" and the Raman Spectroscopy were used in order to understand the number and position of holes covered with graphene membranes. The obtained results are then presented. Firstly, the positive aspects and defects of the samples produced by the two types of processes are presented in order to select the process which actually led to the best results. Then, all the vibrational measurements in the frequency domain performed on the membranes by using the Vibrometer are reported, with a focus on the eigenfrequencies of the graphene drums and their Q factor

and tension level. This leads to the discussion chapter were the results obtained on the different samples are compared and carefully studied. It is also highlighted the appearing of the mode splitting in the study of the graphene drums which depends on the quality of the membrane produced. In fact a membrane presenting cracks on the surface would show the break of the symmetry and consequently the splitting of frequency modes. This phenomenon can then be used to evaluate the quality of the fabricated graphene membrane. Indeed, while a ruined membrane would present splitted modes, an intact membrane would present ideal eigenfrequencies as obtained with the circular membrane theory. In this way it is possible to obtain a qualitative analysis of the graphene membrane directly from the frequency spectrum, without using expensive and time consuming techniques like Scanning Electron Microscope (SEM) or Vibrometer in "White light Mode".

Chapter 1

Graphene properties and applications

1.1 Introduction to graphene

Graphene is an allotropic state of carbon and it is by definition a single layer of carbon atoms arranged in an hexagonal lattice. Graphene is the basic constituent of graphite and is also the fundamental element of other low dimensional materials such as fullerene, nanoribbons and nanotubes, as shown in [1].

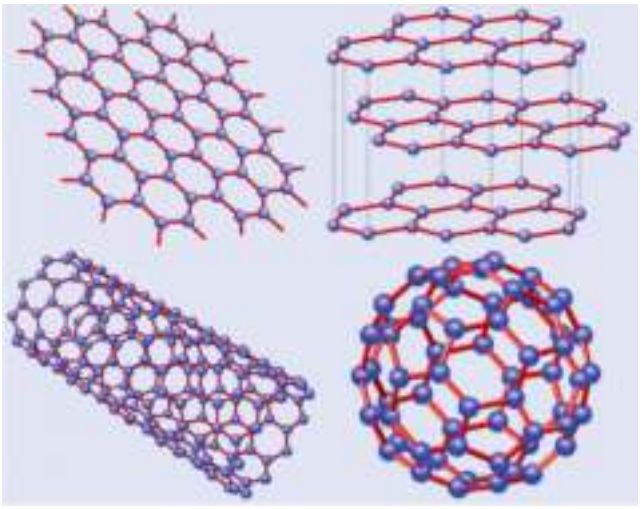

Figure 1.1: Allotropes of Carbon [29]

Despite having been discovered in 1962 by Hanns−Peter Boehm. Many of its 2D properties are still unknown today, this is due to the fact that it was not easy to obtain free-standing graphene. Fortunately, thanks to an experiment made by to scientists from Manchester called "Friday evening experiments" [2], nowadays it's possible to isolate graphene from it's environment. This new method discovered in 2010 Dr. Andre Geim and Dr. Kostantin Novoselov, it initiated graphene research.

1.1.1 Crystal Structure and Electronic Band Structure of Graphene

Graphene has a honeycomb lattice structure and it's first Brillouin zone are shown in Fig(1.2), respectively. In the following description it's important to consider different vector related to the geometry of the lattice of graphene itself. One has the translation vectors $\boldsymbol{a} = a(1,0)$ and $\boldsymbol{b} = a(-1/2, \sqrt{3}/2)$, and the vectors that are related to the nearest neighbor carbon atoms $\boldsymbol{t}_1$ =a $(0,1/\sqrt{3})$,$\boldsymbol{t}_2$ = a(-1/2,-1/2$\sqrt{3}$), and $\boldsymbol{t}_3$ = a(1/2,-1/2$\sqrt{3}$), where a is the lattice constant given by a = 0.246 nm.

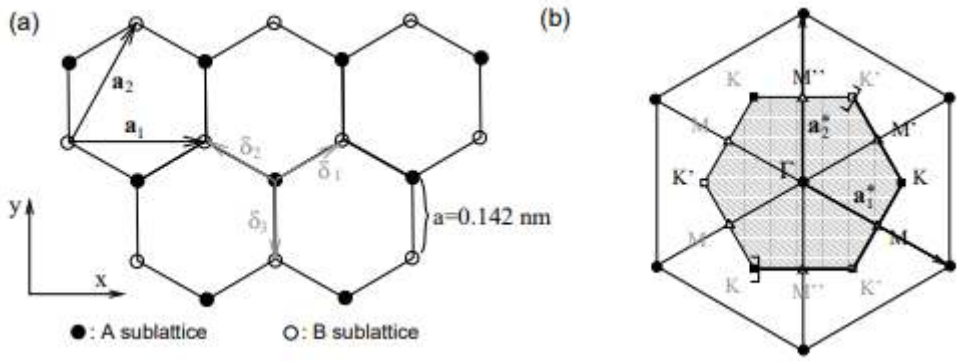

Figure 1.2: Honeycomb lattice structure and the first Brillouin zone of graphene [30]

Graphene has a unit cell that has an area $\Omega_0 = (\sqrt{3}/2)a^2$ with two carbon atoms, that are usually called A and B. Another fundamental vectors are the so called the primitive reciprocal lattice vectors $\boldsymbol{a}^*$ and $\boldsymbol{b}^*$ that have the form : $\boldsymbol{a}^* = (2\pi/\mathrm{a})(1,1/\sqrt{3})$ and $\boldsymbol{b}^* = (2\pi/\mathrm{a})(0,2/\sqrt{3})$. Graphene has an hexagonal first Brillouin zone with an area $\Omega_{0^*} = (2/\sqrt{3})(2\pi/\mathrm{a})^2$. Two points are fundamental in the graphene analysis and they are K and K', that are positioned at the corners of the first Brillouin zone, they assume the form $\boldsymbol{K} = (2\pi/\mathrm{a})(1/3,1/\sqrt{3})$ and $\boldsymbol{K'} = (2\pi/\mathrm{a})(2/3,0)$. Now, in order to analyze the electronic properties of graphene, one has to consider that the conduction and the valence bands are formed only by the π states, and not by the σ states that are more bounded. The K and K' points are touched by the π states where it's located the Fermi level. In order to make a good description of the electronic properties of graphene, one has to consider a tight-binding approach where the wave functions takes the form

$$\psi(\boldsymbol{r}) = \sum_{\boldsymbol{R}_A} \phi_A(\boldsymbol{r} - \boldsymbol{R}_A) + \sum_{\boldsymbol{R}_B} \phi_A(\boldsymbol{r} - \boldsymbol{R}_B) \tag{1.1}$$

the wavefunction $\phi(\boldsymbol{r})$ is related to the p_z orbital located at the origin, having $\boldsymbol{R}_A = n_a\boldsymbol{a} + n_b\boldsymbol{b} + \boldsymbol{t}_1$ and $R_B = n_a\boldsymbol{a} + n_b$. Now, introducing the so called transfer integral $-\gamma_0$, that is between two nearest neighbor atoms and also imposing the energy

origin at one p_z level. One can write

$$\epsilon\psi_A(\boldsymbol{R}_A) = -\gamma_0 \sum_{l=1}^{3} \psi_B(\boldsymbol{R}_A - \boldsymbol{t}_l) \tag{1.2}$$

$$\epsilon\psi_B(\boldsymbol{R}_B) = -\gamma_0 \sum_{l=1}^{3} \psi_A(\boldsymbol{R}_B - \boldsymbol{t}_l) \tag{1.3}$$

for simplicity here the overlap integral between the two sites A and B is neglected. Now, taking into account : $\psi_A(\boldsymbol{R}_A) \propto f_A(\boldsymbol{k})(\boldsymbol{k})exp(i\boldsymbol{k}\,.\,\boldsymbol{R_A})$ and
$\psi_B(\boldsymbol{R}_B) \propto f_B(\boldsymbol{k})exp(i\boldsymbol{k}\,.\,\boldsymbol{R_B})$, one obtains

$$\begin{pmatrix} 0 & h_{AB}(\boldsymbol{k}) \\ h_{AB}(\boldsymbol{k})^* & 0 \end{pmatrix} \begin{pmatrix} f_A(\boldsymbol{k}) \\ f_B(\boldsymbol{k}) \end{pmatrix} = \epsilon \begin{pmatrix} f_A(\boldsymbol{k}) \\ f_B(\boldsymbol{k}) \end{pmatrix} \tag{1.4}$$

where

$$h_{AB}(\boldsymbol{k}) = -\gamma_0 \sum_{l} exp(-i\boldsymbol{k}\,.\,\boldsymbol{t}_l) \tag{1.5}$$

Now it's possible to write the two energy bands that take the form :

$$\epsilon_{\pm} = \pm\gamma_0 \sqrt{1 + 4\cos\frac{ak_x}{2}\cos\frac{\sqrt{3}ak_y}{2} + 4\cos^2\frac{ak_x}{2}} \tag{1.6}$$

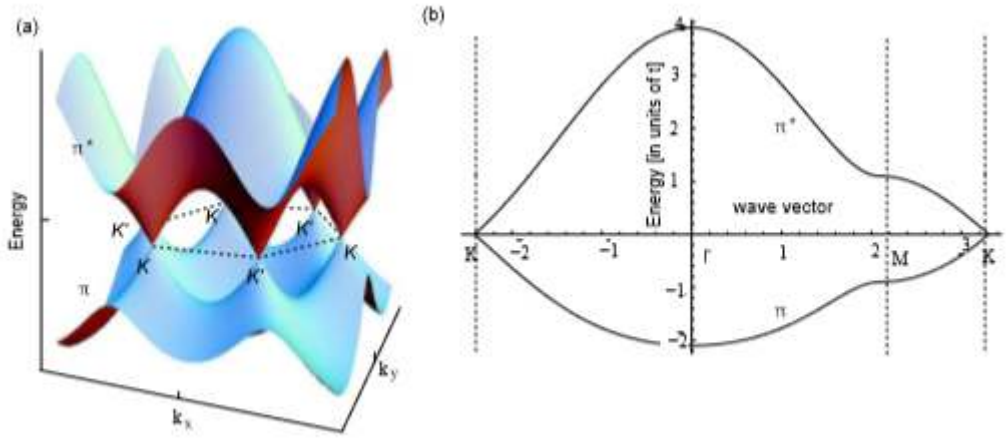

Figure 1.3: Valence and conduction bands of graphene [30]

In Fig(1.3) are shown the valence and conduction bands of graphene. Considering that the electronic properties of graphene are strictly in the proximity of the K point, one has to write $\boldsymbol{k}$ with $\boldsymbol{K}+\boldsymbol{k}$. Considering also the lowest order in $|\boldsymbol{k}|a$, one obtains

$$-\gamma_0 \sum_{l=1}^{3} exp[-i(\boldsymbol{K}+\boldsymbol{k})\,.\,\boldsymbol{t}_1] = -i\omega^{-1}\gamma(k_x - ik_y) \tag{1.7}$$

with

$$\gamma = \frac{\sqrt{3}a\gamma_0}{2} \tag{1.8}$$

Obviously a very similar expression can be obtained for the K' points. Now, having $\epsilon_{\pm}(\boldsymbol{K}) = \epsilon_{\pm}(\boldsymbol{K'}) = 0$, it's evident that no gap is present at K and K' points. Considering that $f_A(\boldsymbol{K}+\boldsymbol{k}) = \tilde{f}_A(\boldsymbol{k})$ and $f_B(\boldsymbol{K}+\boldsymbol{k}) = i\omega\tilde{f}_B(\boldsymbol{k})$

$$\gamma \begin{pmatrix} 0 & k_x - ik_y \\ k_x - ik_y & 0 \end{pmatrix} \begin{pmatrix} \tilde{f}_A(\boldsymbol{k}) \\ \tilde{f}_B(\boldsymbol{k}) \end{pmatrix} = \epsilon \begin{pmatrix} \tilde{f}_A(\boldsymbol{k}) \\ \tilde{f}_B(\boldsymbol{k}) \end{pmatrix} \tag{1.9}$$

one can rewrite the above formula in such way :

$$\gamma(\boldsymbol{\sigma}\,.\,\boldsymbol{k})\tilde{f}(\boldsymbol{k}) = \epsilon\tilde{f}(\boldsymbol{k}), \quad \tilde{f}(\boldsymbol{k}) = \begin{pmatrix} \tilde{f}_A(\boldsymbol{k}) \\ \tilde{f}_B(\boldsymbol{k}) \end{pmatrix} \tag{1.10}$$

with the $\boldsymbol{\sigma} = (\sigma_x, \sigma_y)$ that are the so called the Pauli matrices. Obviously one can obtain the same equation for the K' point, the only object that has to be substituted is $\boldsymbol{\sigma}$ with $\boldsymbol{\sigma}^*$. Now it's possible to write

$$\epsilon_S(\boldsymbol{k}) = S\gamma|\boldsymbol{k}|, \quad (S = \pm 1) \tag{1.11}$$

one now can obtain the density of states

$$D(\epsilon) = \frac{g_s g_v}{A} \sum_{s,\boldsymbol{k}} \delta(\epsilon - S\gamma|\boldsymbol{k}|) = \frac{g_S g_V |\epsilon|}{2\pi\gamma^2} \tag{1.12}$$

having system area A, $g_s = 2$ is the spin degeneracy and $g_v = 2$ is the degeneracy associated to the valley. Due to the fact that the density of states vanishes at the so called Dirac point where $\epsilon = 0$, graphene is often called a zero-gap semiconductor. One can also notice that the energy dispersion relation near the Dirac points it's linear similarly to the photon dispersion relation. This means that the electrons near these to points have an effective mass that is zero, in fact they have a velocity that is about 1/300 the speed of the light.

1.2 Mechanical properties of graphene

Graphene has mechanical properties that distinguish it much different from any thin-film material used today in MEMS and NEMS technology. The $C - C$ bond length is about 0.142 nm, as shown in the previous section , while its interplanar distance in the graphite corresponds to 0.335 nm. Today, moreover, many mechanical properties of graphene are known thanks to measurements carried out by the Atomic Force Microscope (AFM) on freely suspended graphene drums, as shown in [4].

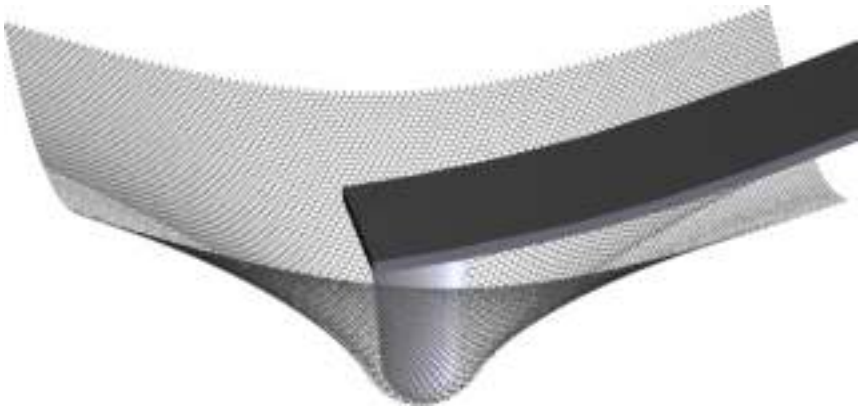

Figure 1.4: AFM tip over graphene membrane [31]

These show that graphene has low mass density of graphene $\rho = 7.4$ x 10^{-19} kg $/\mu m^2$, a two−dimensional in plane elastic stiffness of 340 N/m, that corresponds to a Young's modulus E of 1 TPa. The break of graphene is deeply inside the nonlinear elastic regime, that leads a breaking strength of 42 N/m, that corresponds to a bulk value of 130 GPa. Furthermore these peculiar properties lead to resonant frequencies in a range of MHz.

1.3 Graphene NEMS (GNEMS)

In 1959 Richard Feynmann, during one of his famous lecture [5], talked about how it would be possible in the future to manipulate atomic-scale matter to his liking. What the famous physicist was talking about was precisely what is now called the field of Nanotechnology. In fact, nowadays the NEMS constitute the next phase of miniaturization of the micro-electromechanical systems, the so called MEMS, which generally integrate a nanoelectronics to mechanical actuators, and can thus form amazing physical, biological and chemical sensors. These devices have a low mass, high frequencies of mechanical resonance, quantum mechanical effect, and a high surface / volume ratio [6]. Some of them are accelerometers or detectors of chemicals agent that are present in the environment. Today there are two different and complementar approach that are used in order to build these devices. The first one is called Top-Down while the second one is called Bottom-Up.

- The top-down approach it's also the traditional methods that was used in the fabrication of MEMS. The lithographic process is fundamental in the fabrication of devices, that can be electron beam or optical lithography. These means that this technique is limited by the resolution of the lithographic step. Normally the devices that are fabricated with the Top-Down method are composed by metal films or semiconductor etched layers.

- The Bottom-up approach is the complementary technique of the Top-Down. This uses the chemical properties of the matter in order to produce single molecule that can to self-organize or self-assemble obtaining some useful configuration or conformation. The principle corresponds to the molecular recognition. This technique permits to build and fabricate much smaller structures, having also a good control on the fabrication process.

- A combination of these approaches can be also used, in which nanoscale molecules are added into a top-down structure. An example corresponds to the carbon nanotube that leads to a nanomotor.

Due to its magnificent properties, carbon is the best material used in NEMS technology. The materials that are largely used are carbon nanotubes and graphene. They are used precisely for their chemical properties that leads to higher stability of NEMS, but they are also useful taking into account their peculiar conductivity.
Focusing on what are the so called graphene NEMS (GNEMS), it is possible to notice that there are a large number of possible applications in the literature, in different fields. For instance :

- As shown in [7][8], two applications of graphene resonators are ultralow mass detection and ultrasensitive force detection. In [9], low tension graphene drums for electromechanical pressure sensing are fabricated, where they study the resonant frequency shifts in the presence of helium gas and demonstrate a sensing capability of 1 Torr pressure in a cryogenic environment.

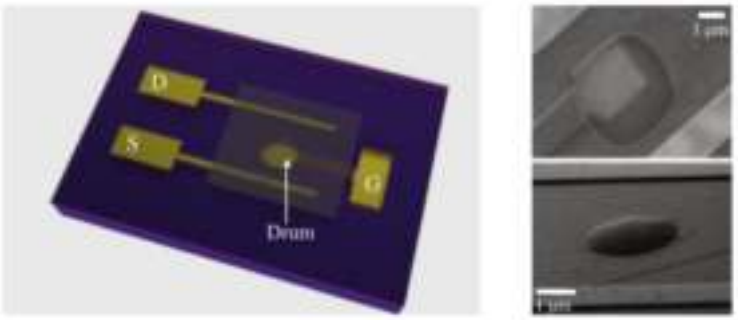

Figure 1.5: Low tension graphene drums for electromechanical pressure sensing [9]

- In [10], is reported the observation of bright visible light emission from electrically biased suspended graphene devices strong optical interference between the suspended graphene and substrate can be used to tune the emission spectrum. Their results pave the way towards the realization of commercially viable large-scale, atomically thin, flexible and transparent light emitters and displays with low operation voltage and graphene-based on-chip ultrafast optical communications

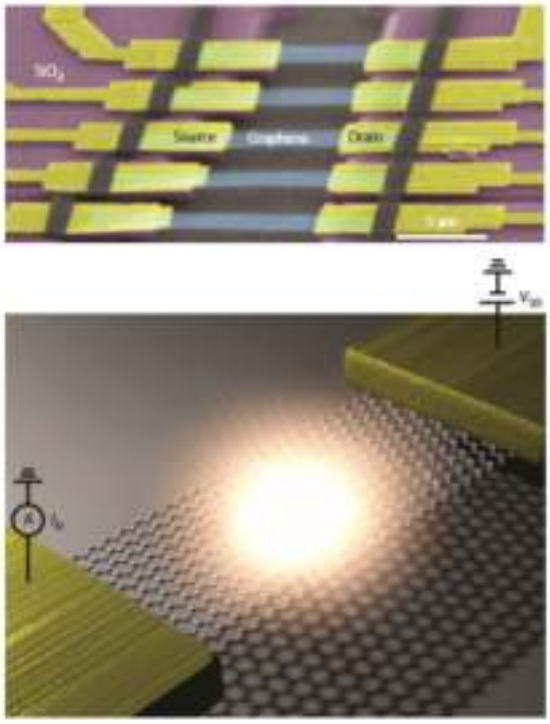

Figure 1.6: Bright visible light on graphene sheets [10]

- In [11] shown that while conventional oscillators typically consist of macroscopic mechanical resonators such as quartz crystals, which require excessive off-chip space. The prototype graphene voltage-controlled oscillators exhibit frequency stability and a modulation bandwidth sufficient for the modulation of radiofrequency carrier signals. As a demonstration, they use a graphene oscillator as the active element for frequency-modulated signal generation and achieve efficient audio signal transmission.

- As shown in [12], they engineer a graphene resonator with large frequency tunability at low temperatures, resulting in a large intermodal coupling strength and they observe the emergence of new eigenmodes and amplification of the coupled modes using red and blue parametric excitation, respectively. Demonstrating that the dynamical intermodal coupling is tunable. This ability to dynamically control the coupling between the high-frequency eigenmodes of a mechanical system opens up the possibility of quantum mechanical experiments at low temperatures.

- In [13], is shown that GNEMS are so suitable also in biological and chemical detection, in fact they have the possibility to become single-molecule detection sensors.

Chapter 2

Theory

2.1 Two dimensional bending vibrations

In order to make a good description of two dimensional bending resonators, one has to consider separately the *plates* and the *membranes*. The case of a *plate*, is an ideal one, and is obtained when the flexural rigidity dominates the mechanical behaviour of the system, while the other case of the *membrane* happen when the behaviour of the system is completely dominated by the tensile stress, and the flexural rigidity can be neglected. Today the two dimensional resonators have large interest in the research field. In fact they are so interesting due to their peculiar properties, for instance : they are considered in nano optomechanics applications, having low mass and strong-coupling.

Rectangular Plate

In order to start with a description of a two dimensional system, one has to consider the *rectangular plate*, that has an equation of motion :

$$D_P \nabla^2 \nabla^2 u - \rho \frac{\partial^2 u}{\partial t^2} = 0 \tag{2.1}$$

where D_P corresponds to the flexural rigidity. This equation can be formally solved considering the plate simply supported and making a separation of the two involved variables (spatial and time ones), one can write

$$u(x, y, t) = U(x, y) cos(\omega t) \tag{2.2}$$

the amplitude $U(x, y)$ has a sinusoidal shapes

$$U(x, y) = \sum_{n=0}^{\infty} \sum_{j=0}^{\infty} U_{0,nj} sin\left(\frac{n\pi x}{L_x}\right) sin\left(\frac{j\pi y}{L_y}\right) \tag{2.3}$$

the two side lengths are L_x and L_y, which are related to the x and y directions. Now the eigenfrequencies of the system can be obtained writing

$$\Omega_{n,j} = \pi^2 \sqrt{\frac{D_P}{\rho h}} \left(\frac{n^2}{L_{x^2}} + \frac{j^2}{L_{y^2}}\right) \tag{2.4}$$

and for a quadratic plate the equation above becomes

$$\Omega_{n,j} = \frac{\pi^2(n^2+j^2)}{L^2}\sqrt{\frac{D_P}{\rho h}} \tag{2.5}$$

So, one has to consider that simply supported plates are substantially impossible to create them on the nano scale, in addition this eigenmode problem is so hard to solve due to these boundary conditions. In this case a good approximation can be obtained by using the so called *Rayleigh's method* for the fundamental eigenfrequency. This method consists in checking and calculating the kinetic and potential energies that are :

$$W_{kin,max} = \frac{\omega^2}{2}\rho h \iint U^2 dxdy \tag{2.6}$$

and

$$U_{pot,max} = \frac{1}{2}D_P \iint (\nabla^2 U)^2 + 2(1-\nu)\left[\left(\frac{\partial^2 U}{\partial x \partial y}\right)^2 - \frac{\partial^2 U}{\partial x^2}\frac{\partial^2 U}{\partial y^2}\right] dxdy \tag{2.7}$$

The equation above, for a rectangular plate, gives an exact solution of the fundamental mode with a good approximation

$$U(x,y) = c(x^2 - (L_x/2)^2)^2(y^2 - (L_y/2)^2)^2 \tag{2.8}$$

and the clamped boundary conditions are satisfied by

$$\frac{\partial U}{\partial x_{\pm L_x/2}} = 0 \quad and \quad \frac{\partial U}{\partial y_{\pm L_x/2}} = 0 \tag{2.9}$$

So, inserting into Rayleigh's equation, the mode shapes in (2.8), one obtains a good approximant solution for the fundamental mode

$$\Omega_{1,1} = 6\sqrt{2}\sqrt{\frac{7L_x^4 + 4L_x^2L_y^2 + 7L_y^4}{L_x^4 L_y^4}}\sqrt{\frac{D_P}{\rho h}} \tag{2.10}$$

obtaining for a square plate

$$\Omega_{1,1} = \frac{36}{L^2}\sqrt{\frac{D_P}{\rho h}} \tag{2.11}$$

This can be extend for the general eigenfrequency of a bending plate, which can be written as

$$\Omega_{n,j} = \alpha_{n,j}\frac{1}{L^2}\sqrt{\frac{D_P}{\rho h}} \tag{2.12}$$

Circular Plate

Considering now the *circular plate*, one can directly obtain the fundamental eigenfrequency following the Rayleigh method, having a good approximation. As made for the *rectangular plate*, one has to calculate the potential and kinetic energies that can be write as

$$W_{pot,max} = \pi D_P \int_0^R \left(\frac{\partial^2 U(r)}{\partial r^2} + \frac{1}{r}\frac{\partial U(r)}{\partial r} \right) - 2(1-\nu)\frac{\partial^2 U(r)}{\partial r^2}\frac{1}{r}\frac{\partial U(r)}{\partial r} r dr \tag{2.13}$$

and

$$W_{kin,max} = \pi \rho h \int_0^R (U(r))^2 r dr \tag{2.14}$$

Having the so called clumped boundary conditions, the mode shape function can be correctly approximated by

$$U(r) = c\left(1 - \left(\frac{r}{R}\right)^2\right)^2 \tag{2.15}$$

The following equations $W_{pot,max} \approx 32\pi D_P/(3R^2)$ and $W_{kin,max} \approx \pi h R^2 \rho/10$ are obtained by substituting (2.15) in (2.13) and (2.14), using now the Rayleigh's equation one obtains the fundamental eigenfrequency

$$\Omega_{1,0} \approx 10.33 \frac{1}{R^2}\sqrt{\frac{D_P}{h\rho}} \tag{2.16}$$

Again this can be extended for a general solution for an eigenfrequency problems obtainig :

$$\Omega_{n,j} = \alpha_{n,j}\sqrt{\frac{D_P}{h\rho}} \tag{2.17}$$

with the $\alpha_{n,j}$ coefficents are acquired by using the *Rayleigh method*.

2.1.1 Free bending vibration of plated under tensile stress (Membranes)

Rectangular Membrane

The case of *rectangular membranes* can be correctly described by the following two dimensional equation of motion

$$\sigma \nabla^2 u - \rho \frac{\partial^2 u}{\partial t^2} = 0 \tag{2.18}$$

in order to obtain a solution to this equation, one has to proceed in the usual way used for the plates. Using (2.3) and (2.18), it's possible to obtain the eigenfrequencies that correspond to

$$\Omega_{n,j} = \sqrt{\frac{\sigma}{\rho}}\sqrt{\frac{n^2\pi^2}{L_x^2}\frac{j^2\pi^2}{L_y^2}} \tag{2.19}$$

that in the case of a square membrane becomes

$$\Omega_{n,j} = \pi\sqrt{n^2+j^2}\frac{1}{L}\sqrt{\frac{\sigma}{\rho}} = \pi\sqrt{n^2+j^2}\frac{1}{L}c_\sigma \tag{2.20}$$

This solution it's so similar to the one-dimensional case of a string.

Circular Membranes

Even in the case of a *circular membrane*, one can obtain the approximated eigenfrequencies following the Rayleigh method. Making a change of coordinates, it is possible to describe the mode shapes of a circular membrane in a better way. This choice is related to the system geometry, in fact, in this case, one has to pass to the circular coordinates, where r is the radial coordinate and R is the radius of the membrane

$$U(r) = c\cos\frac{\pi r}{2R} \tag{2.21}$$

In the equation above is represented the fundamental mode, which has an amplitude c. So, following the Rayleigh method one has to check and calculate the maximal kinetic and potential energies that correspond to the following ones

$$W_{kin,max} = \frac{1}{2}\omega^2\rho\int_0^R U(r)^2 2\pi r dr \tag{2.22}$$

and

$$W_{pot,max} = \frac{1}{2}\sigma\int_0^R \left(\frac{\partial U(r)}{\partial r}\right)^2 2\pi r dr \tag{2.23}$$

Using the Rayleigh principle it's possible to acquire with a good approximation the fundamental mode that corresponds to

$$\Omega_{1,0} \approx \frac{\pi}{2}\sqrt{\frac{\pi^2+4}{\pi^2-4}}\frac{1}{r}\sqrt{\frac{\sigma}{\rho}} = \frac{2.415}{R}\sqrt{\frac{\sigma}{\rho}} \tag{2.24}$$

this is so closed to the correct one

$$\frac{2.404}{R}\sqrt{\frac{\sigma}{\rho}} \tag{2.25}$$

Once again it's evident that the approximation obtained via Rayleigh method is correct and in the general case one can write the eigenfrequencies of the circular membrane as

$$\Omega_{n,j} = \frac{\alpha_{n,j}}{R}\sqrt{\frac{\sigma}{\rho}} = \frac{\alpha_{n,j}}{R}c_\sigma \tag{2.26}$$

c_σ is the velocity of a wave moving on the membrane.

2.2 Modes Splitting

Making a deeper analysis of a circular membrane, one can also check the splitting of the modes. In order to investigate this behaviour, one has to consider a membrane with an off-centered discrete stiffness, as shown in [25]. In such case, one can write the equation of motion in this way : considering also that the location of the spring with a constant k are $r = r_0$ and $\phi = 0$

$$-\sigma\nabla^2 u + \rho\frac{\partial^2 u}{\partial t^2} - ku\delta(r - r_0)\delta(\phi) = 0 \tag{2.27}$$

In order to write the approximate soluton, one has to expand a pair of degenerate modes

$$u(r,\phi,t) = g_{(m,n)}(t)U_C^{(m,n)}(r,\phi) + h_{(m,n)}U_S^{(m,n)}(r,\phi) \tag{2.28}$$

having as modal coordinates $g_{(m,n)}(t)$ and $h_{(m,n)}(t)$ that also correspond to the cosine and sine modes and having as eigenfunctions U_C and U_S where C stays for cosine while S stays for sine modes. So, making the inner products individually for every eigenfunctions and making a substitution in the equation of motion one gets

$$\ddot{g}_{(m,n)} + \left[\frac{D_P\gamma_{(m,n)}^2}{\pi\rho} + \frac{2kJ_i^2(\gamma_{(m,n)}r_0)}{\pi\rho b^2 J_{m+1}^2(r_0\gamma_{(m,n)})}\right] g_{(m,n)} = 0 \quad and \quad \ddot{h}_{(m,n)} + \left[\frac{D_P\gamma_{(m,n)}}{\pi\rho}\right] h_{(m,n)} = 0 \tag{2.29}$$

In the equation above, J are Bessel's functions and γ is a term that is proportional to ω. Now it's clear that the pair of degenerate modes is broken. In fact in a more general case, all the degenerate modes are split. This phenomenon that is called "frequency splitting" occurs when the isotropy of the degenerate modes is broken by an interaction that destroy the system symmetry.

Chapter 3

Experimental

3.1 Measurement techniques

In this section, an accurate description of the various measurement apparatus used for sample characterization will be made. These are : the Vibrometer, the Scanning electron microscope and the Raman spectroscopy.

3.1.1 Vibrometer

The Vibrometer is widely used for mechanical measurements of MEMS and NEMS systems. It also has different functionalities, which allow the user to investigate the shape and appearance of the system under examination. More deeply, the vibrometer allows to carry out what are the so called non-contact measurements, this is the reason why it is used in MEMS R&D. These allow the analysis of dynamic and static systems to be carried out to optimize the quality and design of a product. It is also a versatile system, which can be adapted and used for different types of measurements and it can also be assembled and transported in an easier way. In the following section two different but useful tools which are the Surface Metrology and the Scanning laser Vibrometry will be described.

Figure 3.1: A rapresentation of the Polytech PM51 Vibrometer [32]

Surface Metrology

This is an excellent tool that allows to analyze the design of micro and nano structures. In fact, it is possible to investigate the topography of the surface of the sample under examination, in order to be able to identify any defect to eventually improve the quality and performance of micro and nano structures. The user can in fact perform topographic measurements obtaining 3D and 2D profiles to analyze.

Measurements

This type of measurement allows a high resolution along the three Cartesian axes (x,y,z), creating a very accurate and detailed map of the sample in question. This type of measurement is obtained by shifting an interference objective with nanometer precision with respect to the sample. In addition, various parameters can be determined by using this tool, for instance : Flatness, Waviness, Height, Parallelism, Angles, Roughness, Curvatures, Volumes. Both the realization of this type of measurement and the analysis of the following results are easy for an inexperienced user. In fact, the user must follow these simple steps:

- place the sample
- focus the microscope
- define the vertical scan and the exposure time
- start the measurement

Physics

As mentioned above, this system exploits the interference phenomenon that is generated by spreading a reference object in respect to the sample under examination. Interference is generated when two monochromatic and coherent waves are superimposed. Thus constructive or destructive interference can be obtained, depending on the phase difference between the two waves. The interference, which is produced by two superimposed waves, can be experimentally verified by using a Michelson interferometer. In a system of this type the light beam produced by a source is split into two parts by using the so called beam splitter. A ray of light will be directed towards the sample, while the other will be directed towards the reference sample. Subsequently, an interference pattern will be generated by the light that will be reflected both from the sample under examination and from the reference, which can be detected by a camera. The use of monochromatic waves, however, will often lead to inaccurate results, in fact if the surface under analysis is disconnected or has large steps, one must use what is called: "white light". The white light is composed of a very high number of monochromatic waves that have a different wavelength. This explains why using this type of light the interference will be created only on a small range of frequencies. This type of interference is called Correelogram. By analyzing the correelograms after each measuring cycle, the correct topographic representation of the surface of the sample under examination is obtained.

Scanning Laser Vibrometry

This excellent tool allows the user to make real time measurements as well as non-contact measurements in order to analyze and characterize the vibrational behaviour of the sample under examination. In fact one can determine and analyze the vibration displacement and velocity acquired at any sample point. It also has a very high resolution that allows to obtain measurements that have a spatial accuracy of the picometers and a frequency spectra that can reach 24MHz can also be obtained.

Measurements

Even this type of measurement, as the previous one, is simple and intuitive also for an inexperienced user. It is possible to analyze and characterize the entire surface of the sample in a limited time. The vibrometer will scan carefully all the points of the surface selected by the user automatically. Once the entire scan is finished, it will be possible to analyze the frequency spectrum of the sample, obtaining 2D or 3D images, by selecting the examined mode. This allows the user to be able to make an accurate analysis of the sample's behaviour. Moreover, this system has a software with different features like : time domain analysis, FFT, Zoom FFT, averaging and peak hold measurements.

Physics

A Laser Doppler vibrometer measures the Doppler frequency shift of backscattered light from a moving surface. The measurement is performed by comparing the frequency variation between the light reflected (or scattered) by the moving samples under test with the laser beam reflected by a fixed reference mirror and the surface of the samples under test. A waveform generator included in the machine is used to excite the piezoelectric disk, which generates the mechanical vibration to move the nanomechanical sensor. The measure of the beam vibration performed on the middle of the structure is then coupled with the excitation waveform to synchronize the two signals and determine the resonance spectrum of the scanned oscillator. To achieve this particular type of measurement, the physical effect that is taken into account is the doppler effect. In fact a Laser doppler vibrometer measures the frequency shift of light that is reflected by the moving sample. The result of the measurement will be obtained by analyzing the variation in frequency between the backscattered light from the moving sample and the light that has been reflected by the reference mirror that is fixed. The sample under analysis is moved by using this piezoelectric disk. The signal obtained by measuring the vibration on the sample is then coupled to the excitation signal in order to synchronized them, determining the resonance spectrum.

3.1.2 Scanning Electron Microscope

As shown in [18][19], the Scanning Electron Microscope, SEM, as already underlined by the name itself, does not use electromagnetic radiation to do an analysis of the sample surface, but it uses an electron source. These electrons are called primary electrons and they are focused through the use of electromagnetic lenses and deflected by objective lens. They go to imping the sample under examination. The deflection lens are fundamental in order to perform the scan areas of the sample.

Figure 3.2: Scanning electron microscope [33]

The fundamental process is therefore the interaction between the generated electron beam and the sample material. This type of interaction is very complex, in fact X-rays, electrons Auger, electrons backscattered and secondary electrons are produced. By collecting a certain type of electrons it will also be possible to obtain a certain image of the sample, by transforming the electronic signal into an electrical signal which is subsequently amplified and modulated. The magnification is given by the ratio between the size of the image and the size of the region on which the scan has been performed. This leads to a high resolution black-and-white image. This is why SEM images are immediately intelligible and intuitive to understand. The scanning electron microscope can obtain images that appear to be almost three-dimensional even if it is used on relatively large objects (such as an insect). Obviously the SEM works in vacuum in order to eliminate any type of contamination (with pressures below 10^{-3} Pa). Conductive samples can be easily analyzed, whereas non-conductive samples are more difficult to analyze, in fact it is good to perform a metallic coating on them.

SEM Structure

The SEM is composed by[18][19] :

- An electronic source, called Gun, where electrons are produced and accelerated. The Gun produces electrons by thermionic effect, even if there are sources that exploit quantum phenomena such as Field Emission.
- A system of electromagnetic lenses is situated into the central body of the SEM. These lenses allow to focus the electron beam by reducing its diameter. They have a very complex geometry. Furthermore, the lenses are interposed openings, which filter the electrons by reducing the size of the beam. The last lens acts as an objective, by making the scan. However the resolution is related to the beam diameter of the Gun: very small beams lead to high resolutions.
- The SEM possesses special detectors, which collect the electrons that are produced by the interaction between the sample and the primary beam. They can pick up secondary electrons or back scattered electrons (which will be explained later). The observation of the sample is also closely linked to the nature of the electrons that are collected and acquired.

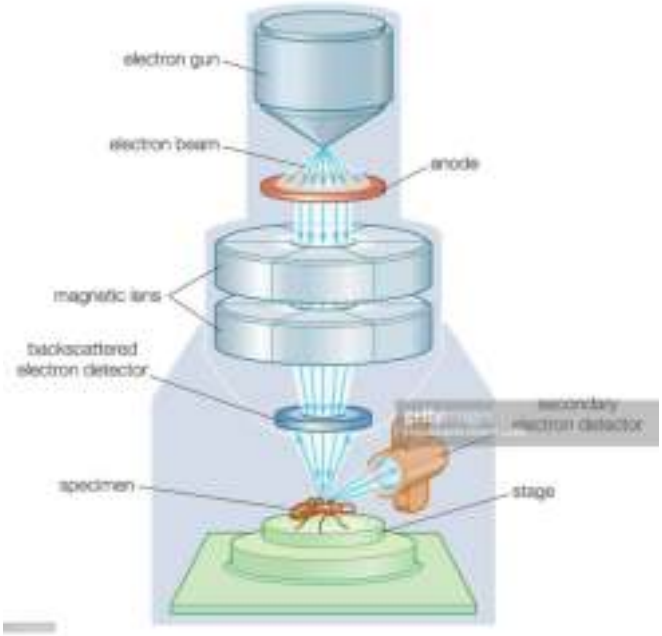

Figure 3.3: SEM structure [34]

Interaction volume

As is well known, the dimensions of the electrons are largely inferior to those of the atoms of which the sample is made. This is why the interaction between the electrons and the sample itself is not only related to the surface but also to several underlying atomic layers. The interaction volume has a pear shape or sphere shape, and it depends on the nature of the sample, precisely from the atomic number Z. If the sample consists

of atoms that have a low atomic number, the interaction volume will be more similar to a pear, close to the surface and tending to widen in depth. If the sample is made up of atoms with a high atomic number, the electrons will face much more difficulty in penetrating the sample. This is why the volume of interaction will be reduced into a sphere of smaller dimensions. In addition, the electrons detected by the sensors can come from different depths of the interaction volume and therefore report different information.
It is possible to distinguish four main zones from which four different types of electrons come:

- Auger electrons: they come from the most superficial areas (1-5 nm depth) and they are released by Auger effect.

- Secondary electrons: having energies between 0 and 50 eV, they come from the surface layers of the massive sample (5-50 nm).

- Backscattered electrons: they have energies close to that of the primary beam (20-30 keV) and they can consequently emerge from regions that are deeper than the volume of interaction (in the order of some hundreds of nm).

- X-Rays: the characteristic X-rays emerge from the deepest region of the interaction volume (in the order of a few microns), with poor spatial resolution compared to the previous signals.

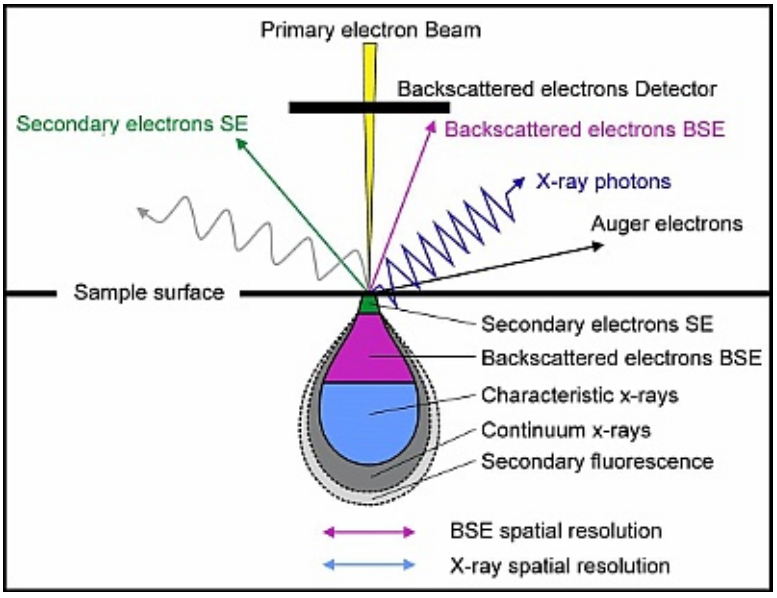

Figure 3.4: Interaction volume of electrons [35]

Backscattered electrons

The backscattered electrons volume of interaction has a large size and it is strictly dependent on the atomic number Z. Backscattered electrons from atoms with high atomic number Z will give rise to a more intense signal, in fact they appear to be lighter on the monitor, unlike those constituted by atoms with smaller darker atomic number Z. These electrons permit also to revial the constituents of the sample, similarly to the Auger electrons.

Secondary electrons

The secondary electron are very important for the high-resolution observation of the sample. They have such a small interaction volume that it permits to detect the smallest details with a resolution corresponding to 5 nm. They also permit to create 3D highly-detailed images.

3.1.3 Raman Spectroscopy

As shown in [20] [21], Raman spectroscopy is widely used in the analysis of samples that can be in different physical phases: both solid and liquid or in gas. This type of measurement is vibrational, it is also a non-invasive technique (the sample is not affected during the measurement). The measurement is obtained in a very short time and the preparation of the measurement does not require any sample preparation. The main effect that is exploited is Raman scattering. The sample is impressed by a monochromatic electromagnetic radiation produced by a laser source. It interacts with the fundamental constituents of the sample, atoms and molecules, by oscillating their electric dipole. Diffuse radiation is fundamental for the aforementioned analysis, in fact it is composed by components with different energies, which are : the Rayleigh component that is related to the elastic diffusion process, no energy is exchanged with the sample, and the Stokes - anti Stokes components that are related to the inelastic diffusion process.

Micro Raman apparatus

It is an apparatus that uses the Raman effect to characterize a particular material. The type of material is identified [20] [21] by measuring the experimental energy shift and comparing it with the phononic energies table .

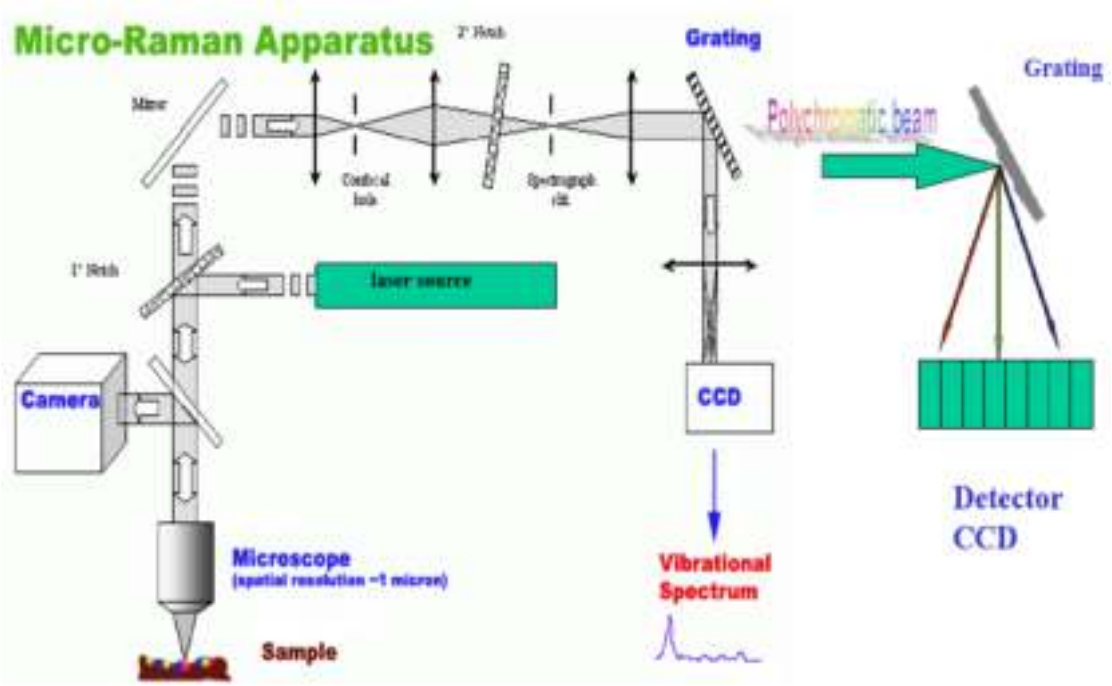

Figure 3.5: Micro Raman apparatus

- An intense, collimable and circumscribable photonic flux source (laser source) is used. Collimable means that it is confined as a cylinder, this characteristic is given by the coherence of the laser source, where the diameter is independent from the distance to which it is projected. Furthermore, the source is almost monochromatic (with a good approximation): there is a set of waves which are very close to each other according to the Fourier analysis, so it can be taken for a monochromatic source. This feature is necessary to evaluate the Raman effect shift: with a polychromatic wave it would have the overlap of all the shifts.

- The first notch filter is set on the chromatic component of the laser, so as to transmit only the light triggered inelastically from the sample, the laser component is instead reflected. The filter is not ideal, so there is a probability of about 10^{-4}, due to the state of the art, that a photon of wavelength equal to that of the source is transmitted. This filter is realized by superimposing different lattices, exploiting interferential effects.

- The spectrophotometer is coupled with an optical microscope to focus the beam at the dielectric limit, in such a way as to optically interrogate the surface of the material in an extremely circumscribed region ($1\mu m$). The defect is that the focused laser produces a very high flow and if the thermal conductivity is noticeably high, it raises the temperature, resulting in crystallizing glassy surfaces for example.

- Then there is a traditional mirror to direct the beam towards a second notch filter which has the same characteristics as the first one and it helps to clean the beam from the residual elastic component. The optical filtration work is made more efficient, in the order of 10^{-8}. The beam thus arrives at a diffraction grating that reflects the different chromatic components at different angles. The polychromatic beam is therefore dispersed in various directions.

- A CCD camera (charge coupled device) is used to realize the vibration spectrum of the excited material, which plots radiation intensity as a function of energy. There will always be residual radiation, so there will be peaks due to inelastic, but also elastic scattering. However, it can be de-emphasized because of spectral different components.

Using this measurement system it is also possible to carry out a stress analysis. This is due to the shift that is visible on the Raman spectrum. The tensile stress causes a red-shift, while a compression stress leads to a blue-shift.

Graphene Raman Spectrum

As shown in literature, for example in [26], the Raman spectroscopy makes it possible to analyze the presence of different materials on a surface as well as the type of stress that may be present. In the study of graphene drums, it is important to recognize the presence of graphene above and near the holes. In fact this type of spectroscopy allows to obtain a large number of information. It is possible to understand from the Raman spectrum : the number of layers, quality, presence of defects, doping, thermal properties and strain. The typical Raman spectrum of graphene possesses different peaks. The three fundamental ones are: the peak D that corresponds to about 1350 cm^{-1}, the peak

G which is about 1580 cm^{-1} and the 2D peak that is around 2700 cm^{-1}. A striking example is shown in [26]. Thanks to Raman spectroscopy, they scan the entire surface, verifying the presence of graphene and its properties. In fact, they reveal the presence of the single layer graphene that is suspended above the holes and they also notice that it becomes more stressed by going closely to them. This is highly visible from the increase of the peak D. Near the hole the graphene totally loses its honeycomb geometry becoming amorphous, whereas far from the hole the graphene has a certain number of defects. This is due to the stress formed during the transfer. A typical Raman graphene spectrum is shown in the figure below

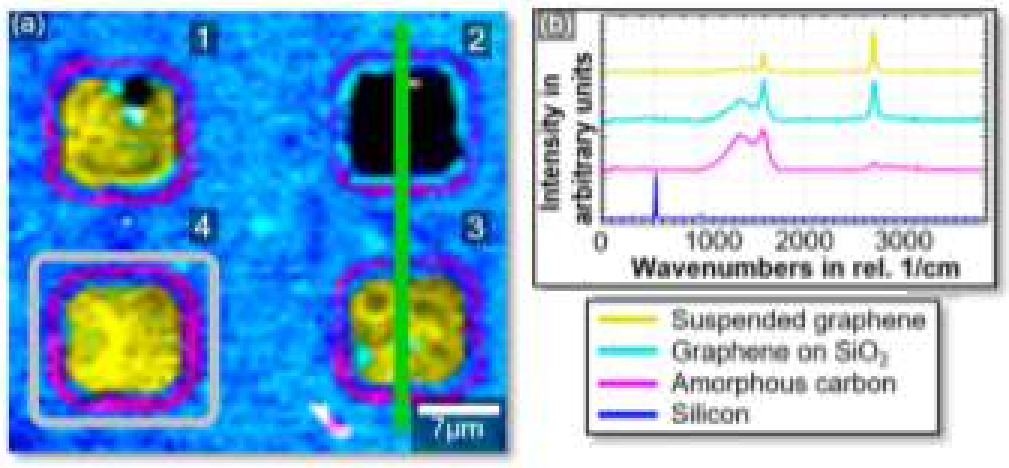

Figure 3.6: Raman Spectrum over graphene drums [26]

3.2 Fabrication of free suspended graphene layer

In this section the entire manufacturing process of the device will be treated. It starts from the deposition of graphene on copper and it continues with the design and the fabrication of the substrate. At the end there is the graphene transfer process.

3.2.1 Graphene on Cu

The most common and simple technique to obtaining graphene corresponds to mechanical exfoliation. It allows to obtain a high-quality graphene, in fact its electronic and mechanical properties are very close to the ideal ones. However the mechanical exfoliation has a big limit: it does not allow to obtain large-sized graphene layers. This problem can be overcome by using Chemical Vapor Deposition (CVD). It is possible to cover large areas by using this method. Graphene can be chemically depositated over different metals, but copper Cu is the best choice as shown in [28].

Figure 3.7: Graphene deposited over Copper via Chemical vapor deposition

The flexible Cu foils are available at low cost. Given the low solubility of carbon in Copper at temperatures around 1000-1500 °C, it is possible to obtain large areas in which deposition of Single layer Graphene (SLG) is predominant. In fact the by layer regions over the surface is over 5%. This process is performed through Chilab in Chivasso. The process follows these steps :

- Graphene was grown on commercial Cu foils (Good Fellow, 25 μm-thick, purity 99.9%) in a cold-wall chemical vapor deposition (CVD) reactor, operating at low

pressure (NANOCVD-8G system from Moorfield). The Cu foils were first cleaned in HCl aqueous solution (10%) for 10 min to remove contaminants and native copper oxide, and air dried.

- After that, pre-heating of the Cu foils was performed at 1000 °C for 10 min under pure Ar flow, and then for 30 s in reducing Ar+H_2 (90%, 10%) atmosphere conditions to further remove Cu oxide residue from the surface.
- The growth of graphene was then carried out at 1000 °C for 300 s, in a mixed atmosphere of Ar (80%), H_2 (10%) and CH_4 (10%).
- The graphene/Cu samples were finally cooled down as fast as possible to 200 °C in reducing Ar+H_2 (90%, 10%) conditions, and then up to room temperature in inert Ar atmosphere.

3.2.2 Substrate Fabrication and Design

As shown in [17], a fundamental step in the design of the entire device is the manufacture of the substrate. First of all it is important to consider the choice of the material, in fact it must have a surface that allows an excellent adhesion to graphene. One of the best choice is the Silicon dioxide SiO_2. So, it is possible to realize the design by knowing the substrate material.
Since a lithography process will be carried out, thanks to the use of a software called Clewin, the mask's design is made. It has circular holes with different diameters ranging from $5\mu m$ to 50 μm.
The whole process is carried out at the Chilab laboratory.

- The first step consists in properly cleaning each slice of SiO_2 with Piranha in order to eliminate any residual dust or other contaminants. Subsequently a spin-coating is carried out in order to obtain a uniform resist with a good adhesion.
- After having adequately performed the lithographic process (having checked that the holes have the correct profiles) it is possible to proceed with the etching of the resist (about 15s).
- Again, after checking that the profiles of the holes correspond to the predetermined values, one can proceed with the etching of the SiO_2 through the use of the BOE 6:1, about 15min for holes with a depth of 1 μm. Wet etching is excellent if one wants to dig holes that have a depth of about 1 μm, but if it is necessary to get holes with a greater depth it is better to use the RIE. The RIE has a decidedly greater Aspect Ratio.

Once the etching is carried out, it is continued with a washing in water. If the dimensions of the holes diameters reflect the pre-established values, the process is finished.

3.2.3 Graphene Transfer

The graphene transfer is the most difficult, critical and delicate step. In fact, the quality of the device depends strictly on it. This step can be done in two ways. The first is a Wet transfer, while the second one is a Dry transfer.

Wet Transfer

As shown in [16][17][37], the Cu foil on which the graphene has been deposited is adequately fixed to the slice of SiO_2 through the use of a tape. This step must be done adequately to obtain an excellent spin coating. The preferable polymer that is largely used in graphene transfer process corresponds to polymethyl methacrylate PMMA.

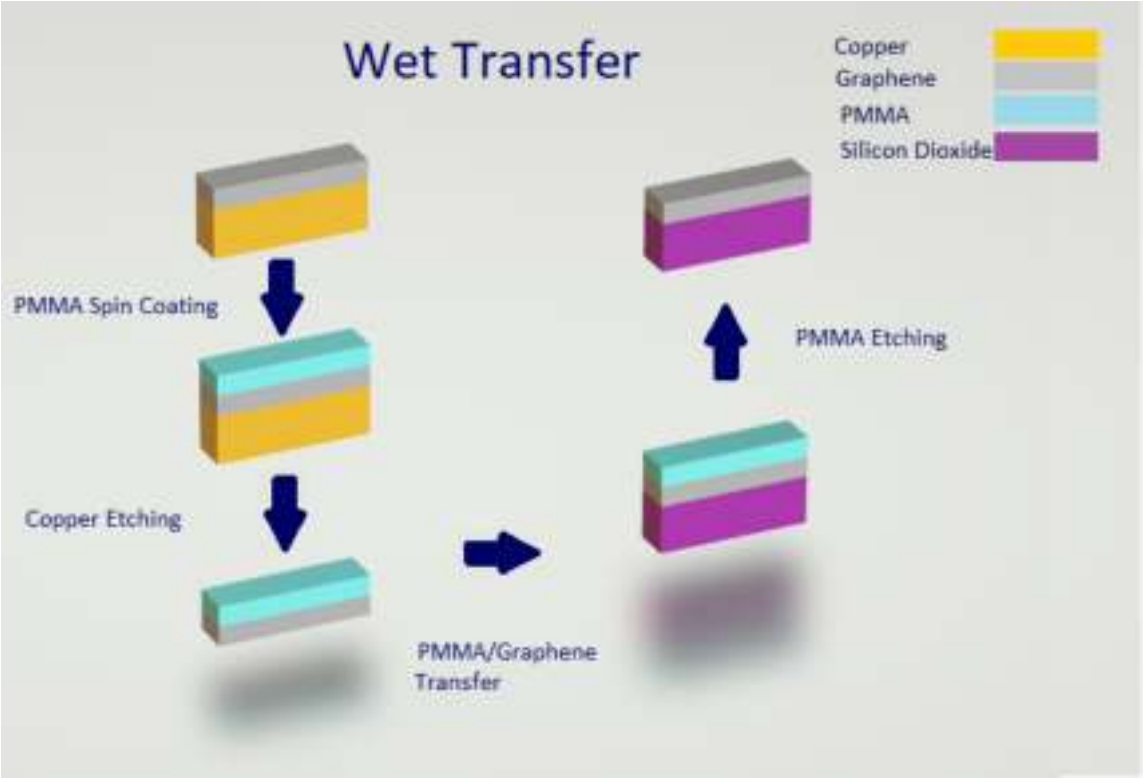

Figure 3.8: Graphene Wet transfer

- The spin-coating is performed with two steps in order to get a width of about 200 nm of PMMA over the Cu/Graphene side. The Spin step is :
  - time 10s, acc 500 m/s^2, RPM 1000
  - time 30s, RPM 1000
- Once the spin step is finished it is important to check that the side of Cu without the graphene has no PMMA residues, because there is the possibility that during the spin, part of PMMA can flow on the back side of the Cu foil. If this happens

the PMMA on the back side must be removed with Acetone using a tip. The coating is performed for three minutes at 150°C.

- The Etching of Cu is now performed. A solution of Ferric Chloride $FeCl_3$ is used. When all the Cu is etched the PMMA/Graphene is drowed out and dipped in a baker with demineralized water for two times. This part of the process is performed because the presence of contaminants of Fe and Cl can be relevant.
- Subsequently the PMMA/Graphene is transferred from the baker with the demineralized water directly on the substrate of interest.
- The final step is the etching of the PMMA. This etching can be performed in two different ways. In fact it is possible to etch the PMMA with a Wet or Dry etching.
  - The Wet etching is performed with the Acetone in a beker.
  - The Dry etching is carried out by evaporating the PMMA. The device is put into furnace at low pressure and in vacuum. When the temperature of 400°C is reached, 300 sccm Ar is fluxed. This is maintained for three to four hours.

Dry etching shows significantly better results than Wet etching.

Dry transfer

As shown in [15][16][36], the Cu foil on which the graphene has been deposited is adequately fixed to the slice of SiO_2 through the use of a tape. This step must be done adequately to obtain an excellent spin coating. The preferable polymer that is largely used in graphene transfer process corresponds to polymethyl methacrylate PMMA.

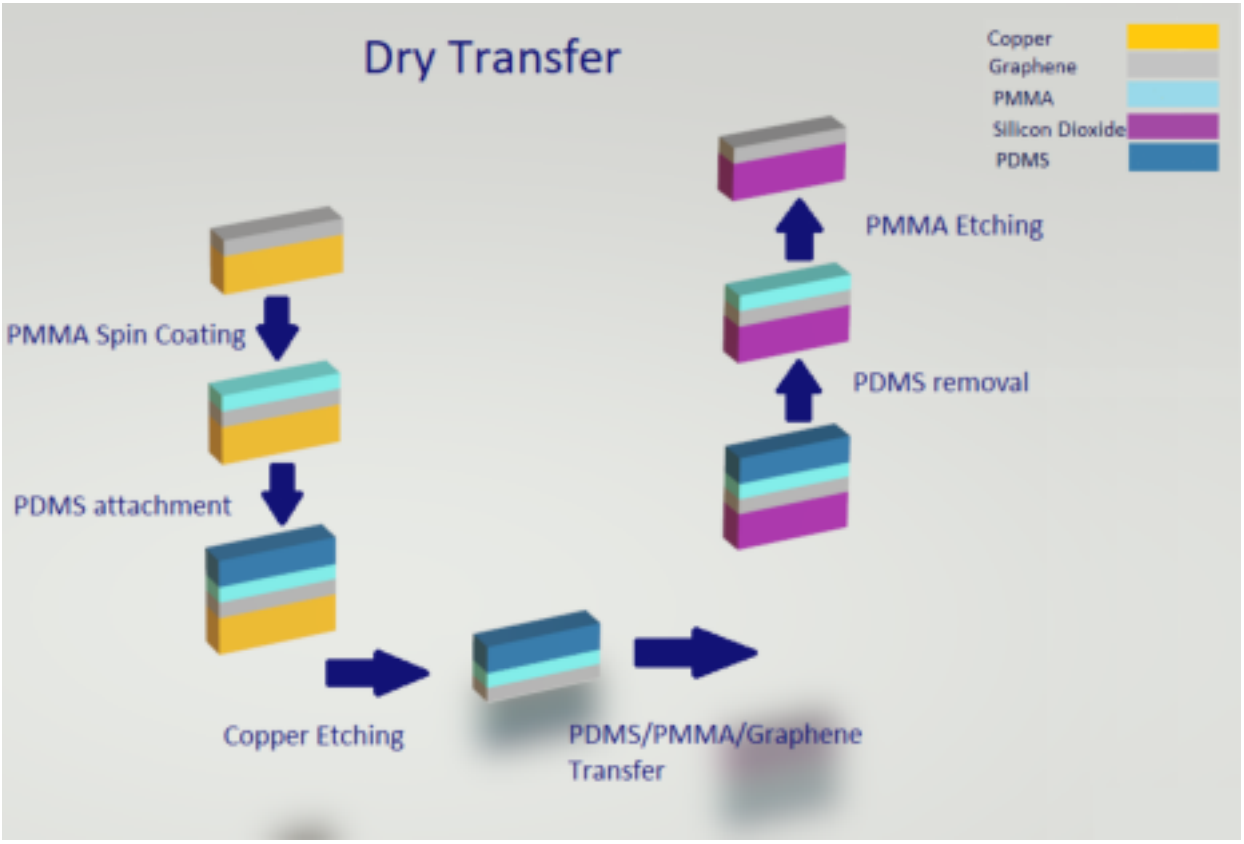

Figure 3.9: Graphene Dry transfer

- The spin-coating is performed with two steps in order to get a width around 200 nm of PMMA over the Cu/Graphene side.
  - time 10s, acc 500 m/s^2, RPM 1000
  - time 30s, RPM 1000
- Once the spin step is finished it is important to check that the side of Cu without the graphene has no PMMA residues, because there is the possibility that during the spin, part of PMMA can flow on the back side of the Cu foil. If this happens the PMMA on the back side must be removed with Acetone using a tip. The coating is performed for three minutes at 150°C.
- After carefully removing the presence of water on the surface of the PMMA, the PDMS is pressed on the PMMA/Graphene in order to obtain an excellent adhesion.

- The Etching of Cu is performed. A solution of Ferric Chloride $FeCl_3$ is used. When all the Cu is etched the PDMS/PMMA/Graphene is drowed out and dipped in a baker with demineralized water for two times. This part of the process is performed because the presence of contaminants of Fe and Cl can be relevant.
- Subsequently the PDMS/PMMA/Graphene is pressed on the substrate and a coating is performed. Heating PMMA over its transition temperature increases the adhesion between graphene and the substrate and after that the PDMS is removed.
- The final step is the etching of the PMMA. This etching can be performed in two different ways. In fact it is possible to etch the PMMA with a Wet or Dry etching.
  - The Wet etching is perfomed with the Acetone in a baker.
  - The Dry etching is carried out by evaporating the PMMA. The device is put into furnace at low pressure and in vacuum. When the temperature of 400°C is reached, 300 sccm Ar is fluxed. This is maintained for three to four hours.

Dry etching shows significantly better results than Wet etching.

Chapter 4

Results

In this chapter the results obtained will be discussed. Firstly the samples that have been manufactured at Chilab and Politecnico di Torino laboratories will be discussed and then the results obtained from the mechanical characterization will be presented.

4.1 Fabricated sample

Several samples were manufactured. They are called G198, G200, G205 , GPDMS, G205n, G211-wet, G211-dry, G217, G218. They were manufactured by two different types of graphene transfer. The first samples are produced via Wet transfer - Wet etching, where the PMMA is removed using Acetone. Given the various problems encountered, it was subsequently decided to try to change the type of transfer, continuing with a Dry transfer - Wet etching approach using the PDMS as a support. Finally, a good compromise was achieved by using a process via Wet transfer - Dry etching, where the PMMA evaporates by using a furnace. This process has allowed to obtain samples that are cleaner and with a vast number of graphene membranes covering the excavated holes.

4.1.1 Sample Wet transfer-Wet Etching

In this section the first samples that are fabricated are described. The substrate was fabricated and designed in the Chilab laboratory. These samples have the same design. Circular holes are excavated with a different diameters that go from 5 μm to 50 μm with a depth of 1 μm. This depth is related to the etching that is an isotropic wet etching using BOE 6:1. The graphene transfer was made from Politecnico di Torino at Limadel. It is a Wet transfer as described in the previous section, with a final Wet etching of the PMMA using Acetone.

Three samples are made with this kind of process. They are : G198, G200 and G205. Due to the impossibility of characterizing them with the "White Light Mode" of the Vibrometer as described in the previous section, it was used a Scanning electron microscope. Given the high quality and resolution of the images obtained from the SEM, it was then possible to carry out a detailed analysis of the samples produced.

G198, G200, G205

These three samples were produced through the same transfer process and they show very similar results. These samples are particularly dirty, with different contaminants and impurities, which are due to the not perfect etching of Copper. Moreover it is possible to notice how in different regions the samples are covered by a polymeric layer, this is due to an imperfect etching of the PMMA using Acetone. A very short number of graphene membranes cover the holes and they are situated in the cleanest region of the samples. These membranes have some defects, they are broken and cracked in some points. In addition, a lot of covered holes have a thick and corrugated membranes, not comparable to the graphene one. This is due to the difficulty of the Wet-transfer process, the graphene has folded itself. In addition, these thicker membranes are broken or splitted as well. These membranes' shape is probably due to the evaporation of the Acetone after the etching of the PMMA that breakes them. All of these aspects are shown in the following figures :

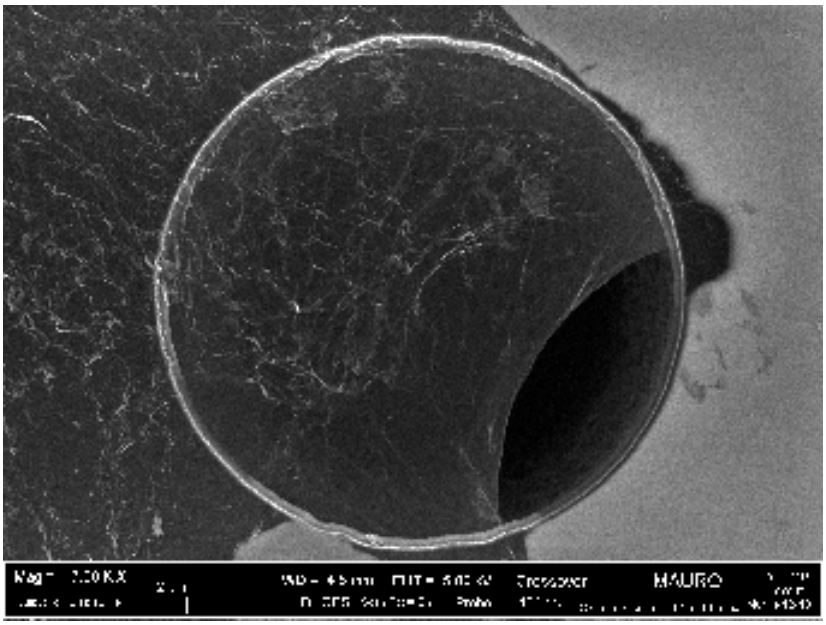

Figure 4.1: Graphene Drum with a folded, corrugated and broken graphene membrane

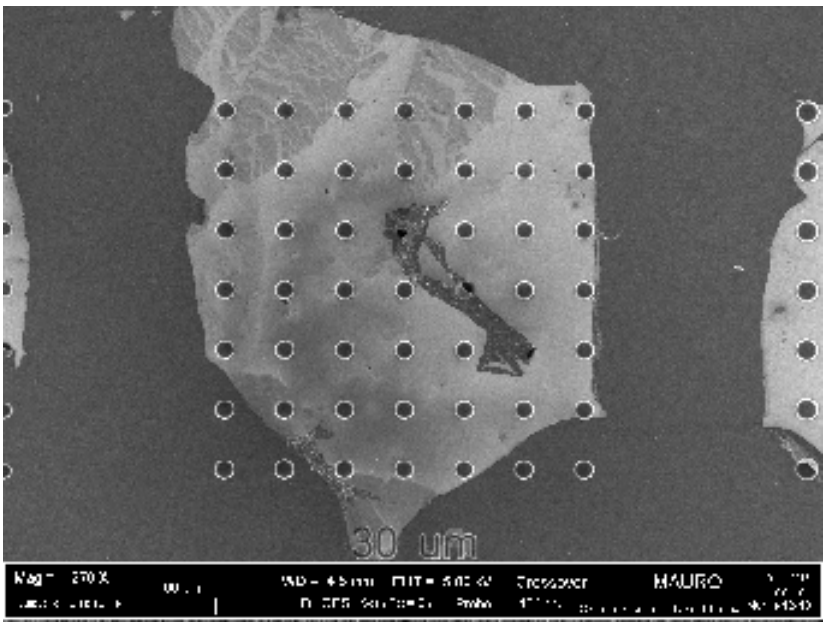

Figure 4.2: Region with holes of $30\mu m$ of diameter, large presence of polymer and folded graphene

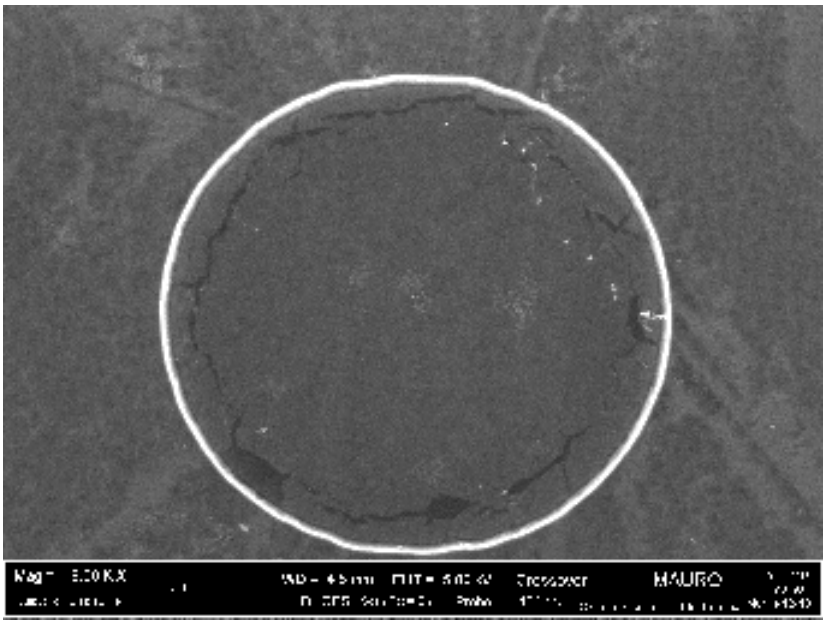

Figure 4.3: Graphene drum with cracked membrane near the edges of the hole

4.1.2 Sample Dry transfer-Wet Etching

In order to overcome the problem described above, a new kind of graphene transfer is developed It corresponds to a Dry transfer as described in a previous section, with a final etching of the PMMA performed via Wet using Acetone. Even in this case three sample are produced, following the same steps. They shows the same results. They are very dirty, with a large presence of contaminants and impurities and there is also a large presence of crystals. Two samples have completely uncovered holes and a lot of their membranes are collapsed inside the holes. Only the third sample shows covered holes.

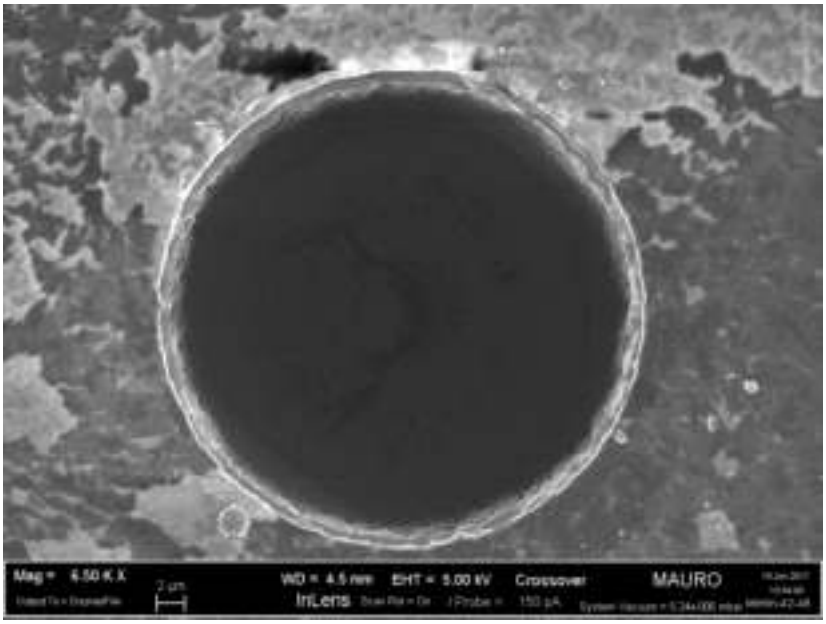

Figure 4.4: Collapsed membrane of graphene inside the hole, a large presence of impurities are presented near the edges

As it is possible to note, newly, there are a very thick membranes that covers the holes, in fact the edges are not so visible. These membranes are also broken and cracked and a large presence of impurities is clearly visible. This is due to the imperfect etching of the Copper. These three samples show the worst results because of the difficulty to realize the Dry-transfer. The most important problem was the presence of the water on the PDMS/PMMA/graphene after the two washes. In fact during the following coating the PDMS go to attachs to the substrate because of the presence of water which, if heated, form very high bound O-H with the SiO_2 substrate.

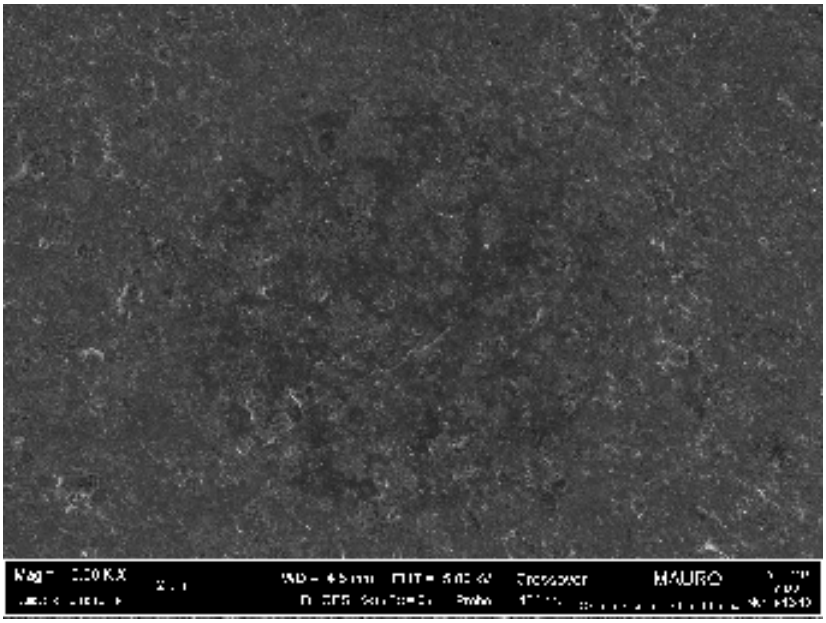

Figure 4.5: Graphene drum with a thick and dirty membrane

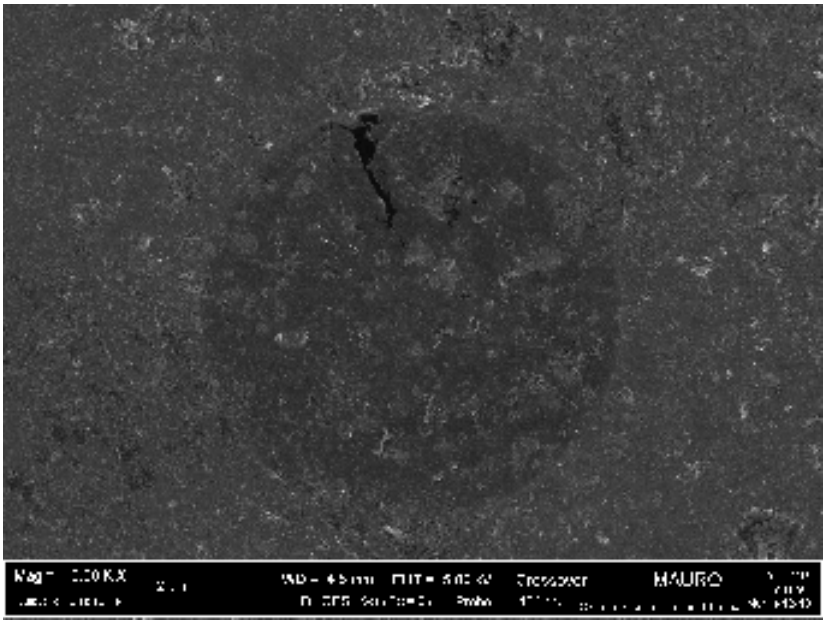

Figure 4.6: Graphene drum with a thick and dirty cracked membrane

4.1.3 Sample Wet transfer-Dry Etching

Due to the worst results obtained by using Dry-transfer as explained above, it was decided to proceed with a Wet-transfer of graphene. Taking into account the problems encountered in the first transfer processes, it was decided to opt for a Dry etching of the PMMA. As discussed in the previous section, the PMMA was etched by using a furnace. The furnace is heated at a temperature of 400°C and it is fluxed for four hours Ar 300sccm. In addition, one sample was fabricated via Wet-transfer Wet-etching, in order to make a strict comparison with the two sample that are produced by following the new Dry step.
These three samples are : G205n, G211-wet, G211-dry

G205n

This sample is produced with the new Dry etching step, it is still partially dirty, with the presence of various contaminants and impurities, but there is a large presence of covered holes. In fact it was possible to carry out a statistics among the surviving membranes compared to the collapsed ones. Moreover, from the geometrical measurements made on the holes, an increase in the hole diameter of 5 μm has been noted. This is due to an incorrect etching time of the Silicon dioxide SiO_2.
This statistics shows that :

Diameter	Percentage
55μm	6%
50μm	10%
45μm	20%
40μm	42,5 %
35 μm	38,75%
30μm	23,25%
25μm	32,4%
20μm	55%
15μm	50,5%
10μm	61,3%

Figure 4.7: Statistic G205

As seen from the statistics, the membrane resistance covering the holes is closely linked to the diameter of the hole itself. The holes that have a diameter of 10 μm have a rate of survival to the process that reaches 60 %, while the holes that have a diameter of 55 μm have a significantly lower survival rate that turns out to be around at 6 %. These membranes are not so thick and corrugated, but also with this new Dry etching of the PMMA they are broken and cracked in different points. In addition, in this case it was also possible to check correctly the presence of a single layer graphene sheets using the Raman spectroscopy obtaining the correct results as represented in the figure below. The presence of the peaks D, G and 2D is clearly visible. The D peak that is related to the presence of defects, is not so peaked. This means that the graphene produced with the Chemical vapor deposition CVD process has a great quality.

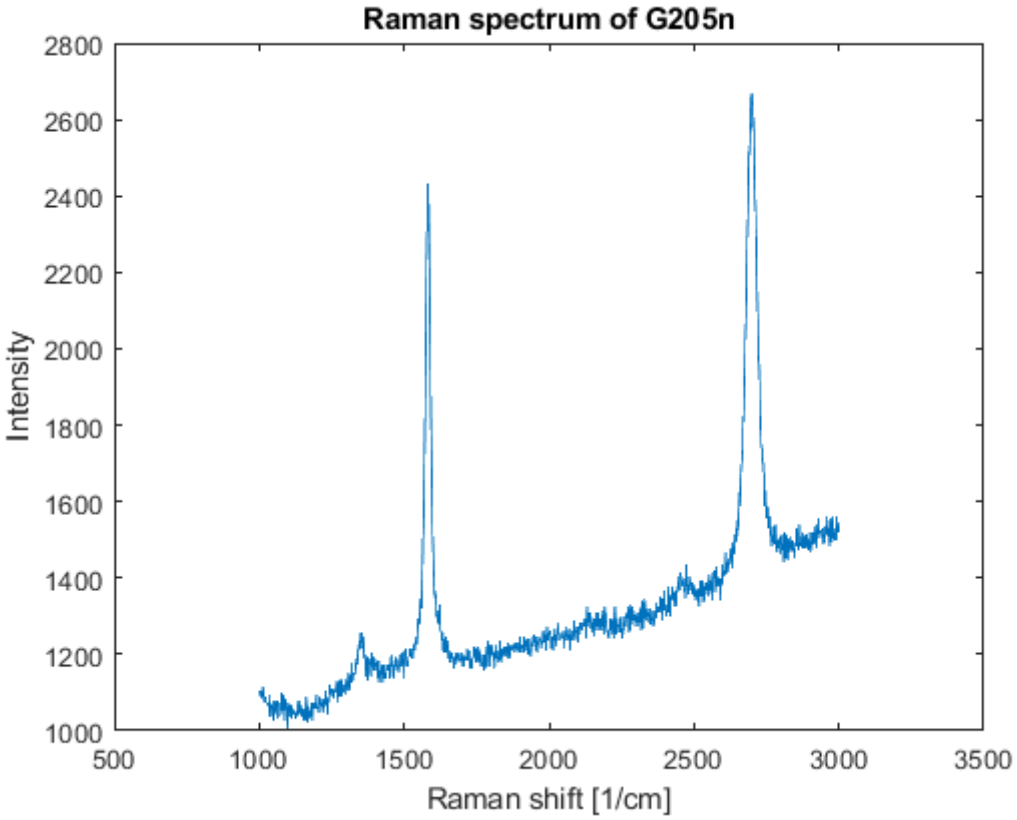

Figure 4.8: Raman spectrum of G205n, obtained over a graphene membrane

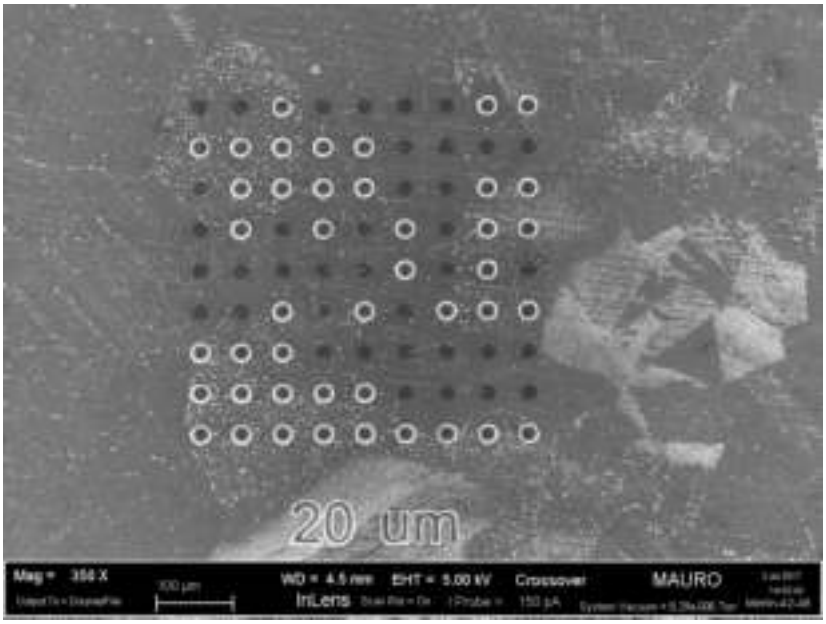

Figure 4.9: Graphene drums of 20μm of diameter, with a large number of covered holes

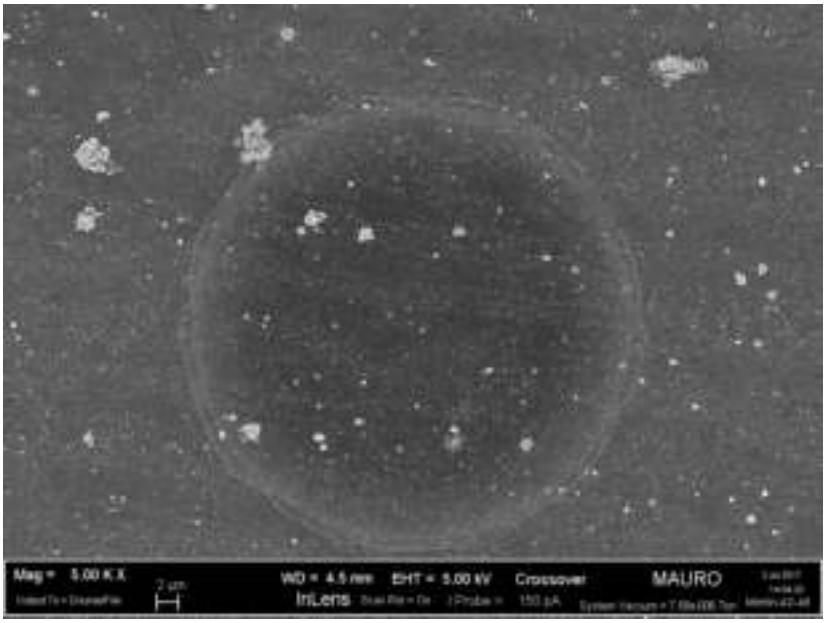

Figure 4.10: Graphene drum of $35\mu m$ with some impurities

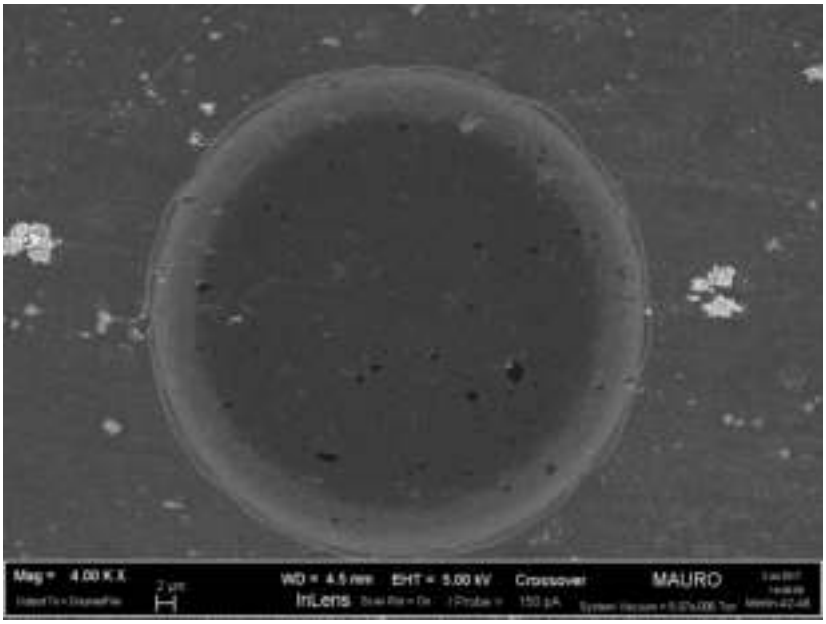

Figure 4.11: Graphene drum of $50\mu m$ with impurties and holes

G211-wet

This sample shows the same characteristics as the first sample produced via Wet-transfer Wet-etching. As it is possible to see in the figure below, the sample results completely uncovered with a large numbers of impurities and contaminants. Only few holes are covered and have thicker and corrugated membranes that are also broken and split in some points.

G211-dry

This sample is not good as G205n but it shows a better quality respect the G211-wet. This sample is not as dirty as G211-wet and it shows to have some membranes that are not so thick and not corrugated, but they are bounded and with a large presence of cracks and splits. Despite the unsatisfactory result, it is evident that the PMMA's Dry etching results much better than Wet etching.

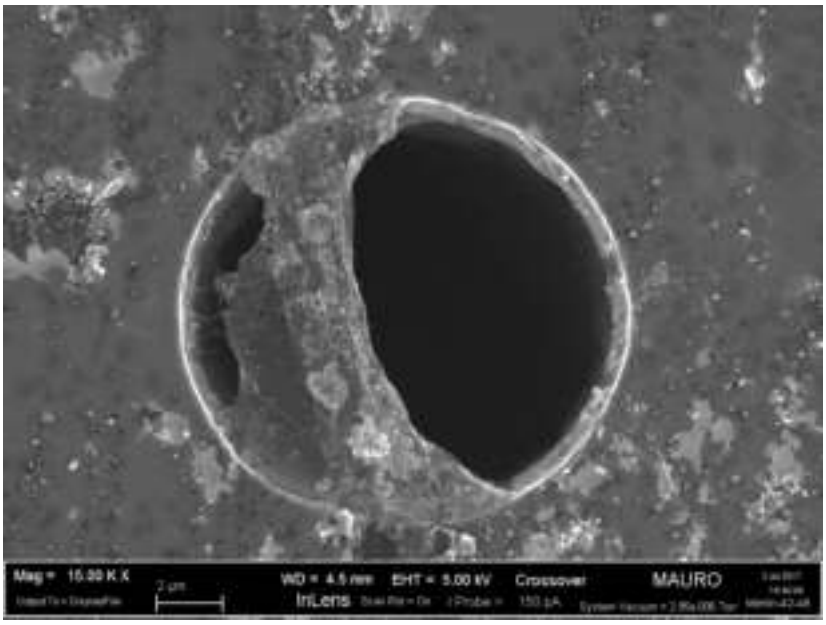

Figure 4.12: G211-wet Graphene drum with a thick, cracked and dirty membrane

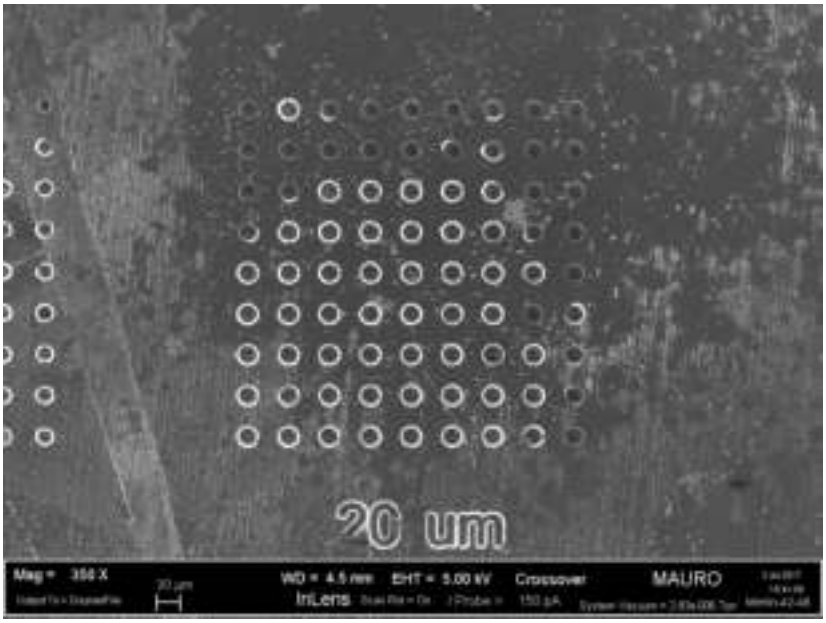

Figure 4.13: G211-wet Region with holes of $20\mu m$, no presence of covered holes

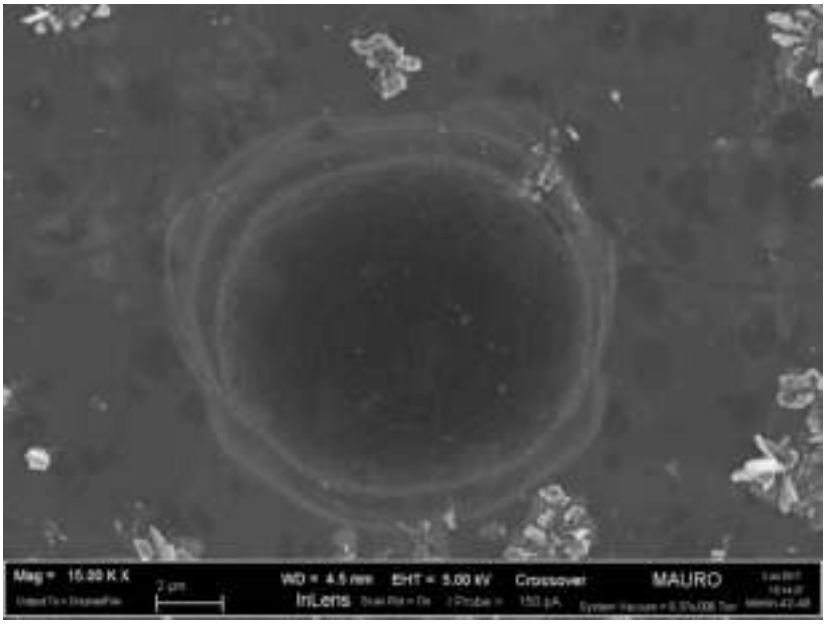

Figure 4.14: G211-dry bounded graphene drum with presence of impurities near the edges

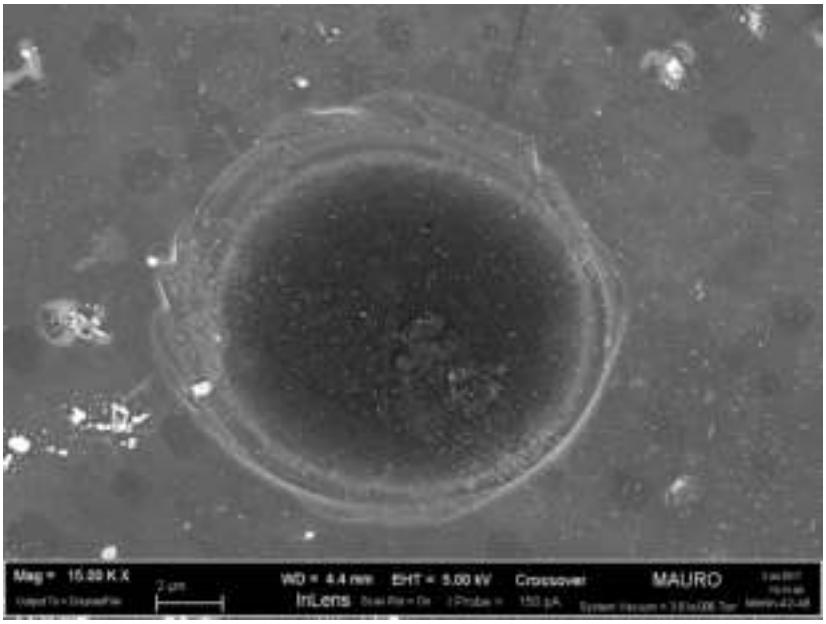

Figure 4.15: G211-dry graphene drum with impurities near the edges

Using this new kind of process Wet transfer - Dry etching, two other samples are fabricated : G217 and G218.

G217

This sample shows several completely covered membranes, but as it is easily visible there is a vast presence of contaminants, impurities and crystals. This presence of dirt is due to the incorrect etching of Copper. It has indeed been possible to notice how the etching of the Copper is proportional to the state of its oxidation. In fact the graphene/Cu used in the fabrication of this device is so old. As it is possible to see the aging of the graphene/Cu day by day

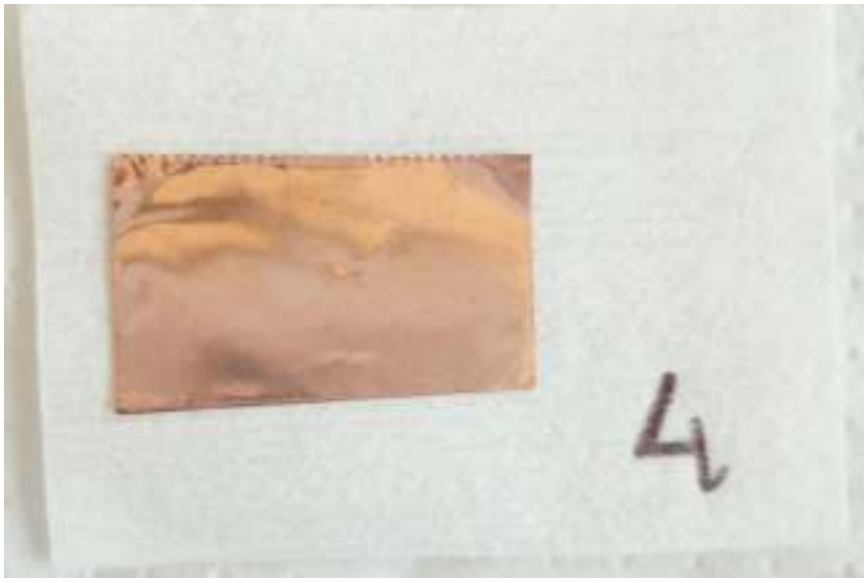

Figure 4.16: Graphene/Cu foil day one

Figure 4.17: Graphene/Cu foil day two

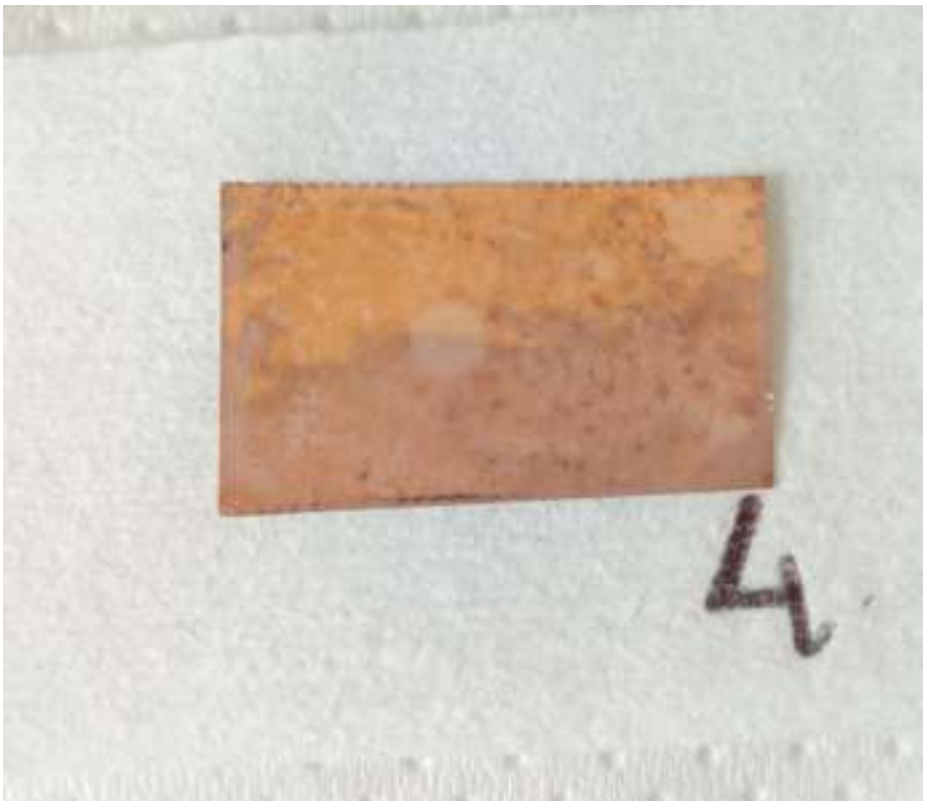

Figure 4.18: Graphene/Cu foil day three

As shown in the figures above, the newly produced graphene/Cu sheet is highly clean and without impurities, but already after 24 hours one notes the presence of black dots and patches that correspond to the oxidation. After 48 hours the graphene/Cu sheet results in even more pronounced and clearly visible black spots. In order to avoid this problem, it was tried to spin and coat the PMMA over the graphene/Cu sheet. But even in this case, the results are identical to the previous ones, after few days the graphene/Cu foil results completely oxidated.

G218

This is the last sample that has been produced. It has been used a new graphene/Cu foil also cleaned with a bath of HCl. It shows great results. This sample results so clean and without a large presence of contaminants and the membranes are not so thick and not corrugated as shown in the figure below. Some of these membranes have some breaks, creeps and split but other membranes do not show them.

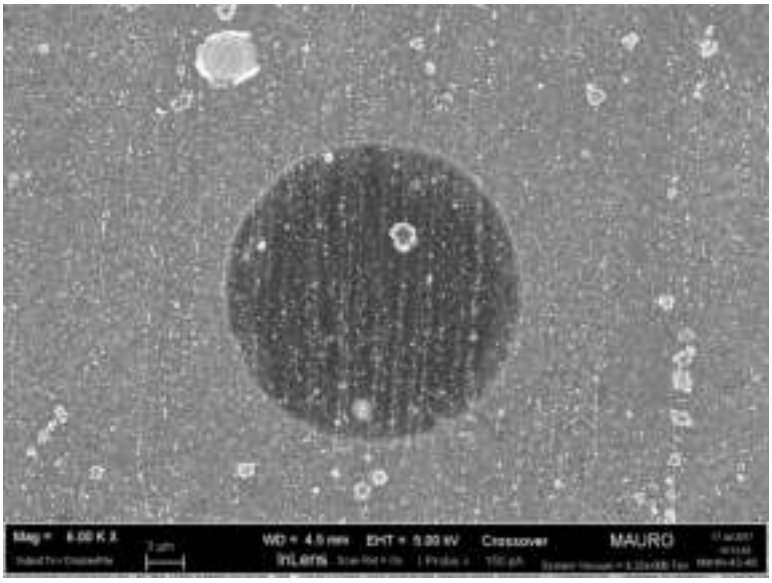

Figure 4.19: G217 Graphene drum with a large presence of impurities

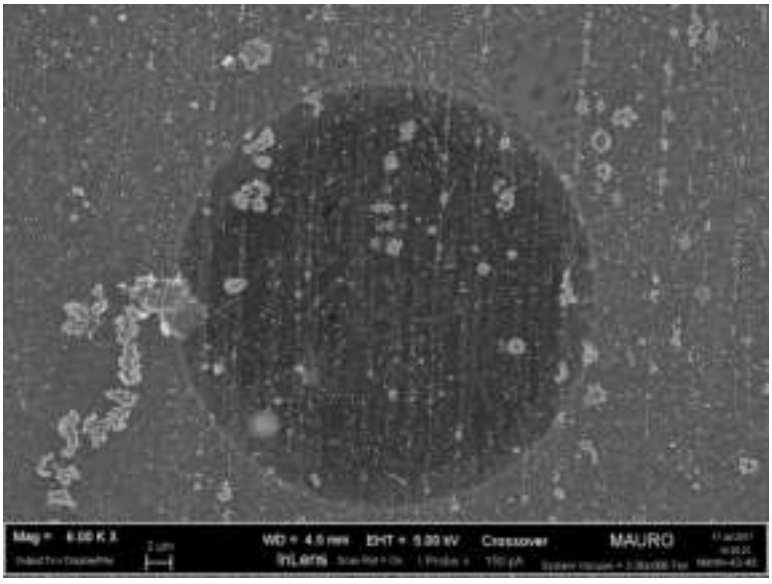

Figure 4.20: G217 Graphene drums with a large presence of impurities and holes

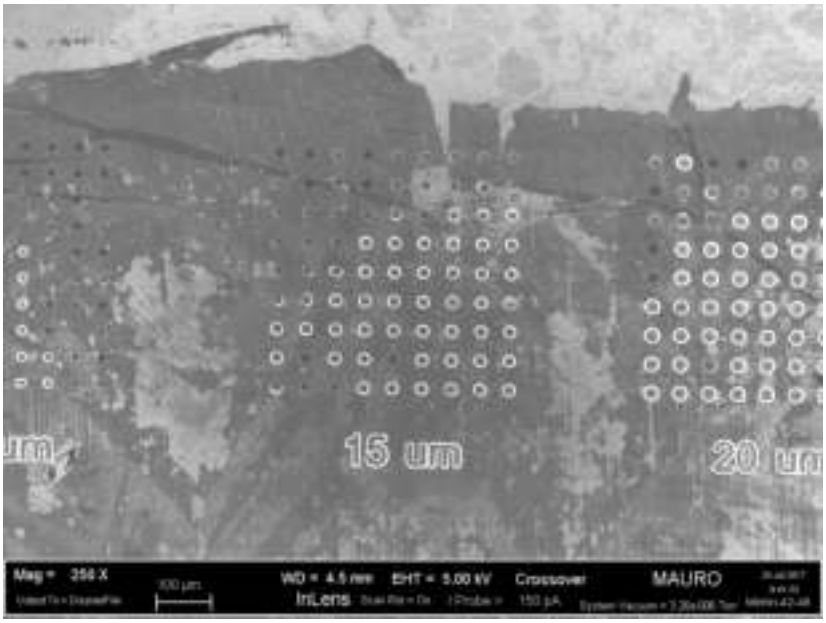

Figure 4.21: G218 Region with different graphene drums, some covered holes are visible

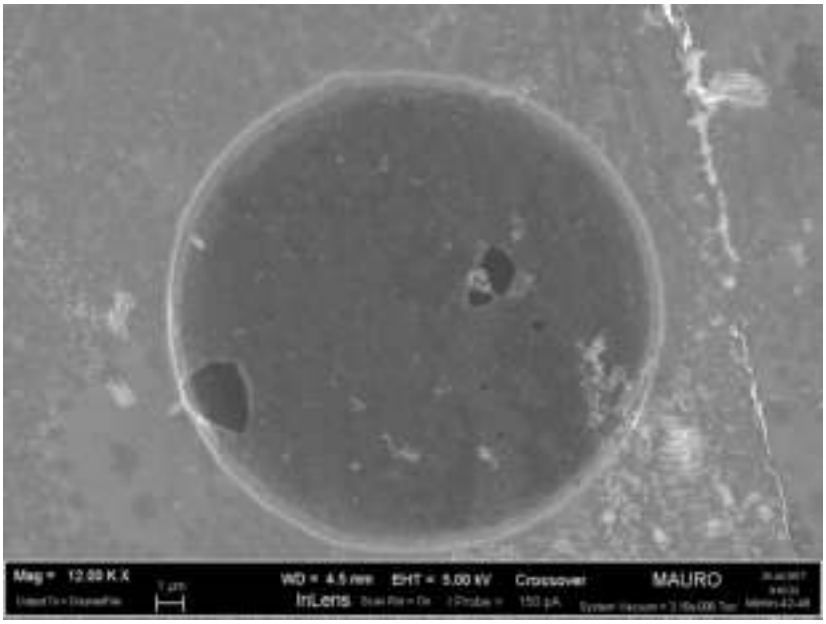

Figure 4.22: G218 Graphene drum with some holes

4.2 Characterization

Three samples are characterized by the use of the Vibrometer at environment temperature, as discussed in the previous section. Thanks to it, it was possible to acquire the frequency spectrum for each measured membrane, without any actuation using only the thermal noise, that it was fundamental in order to check some membrane properties. A typical spectrum of graphene drums obtained by using the Vibrometer corresponds to :

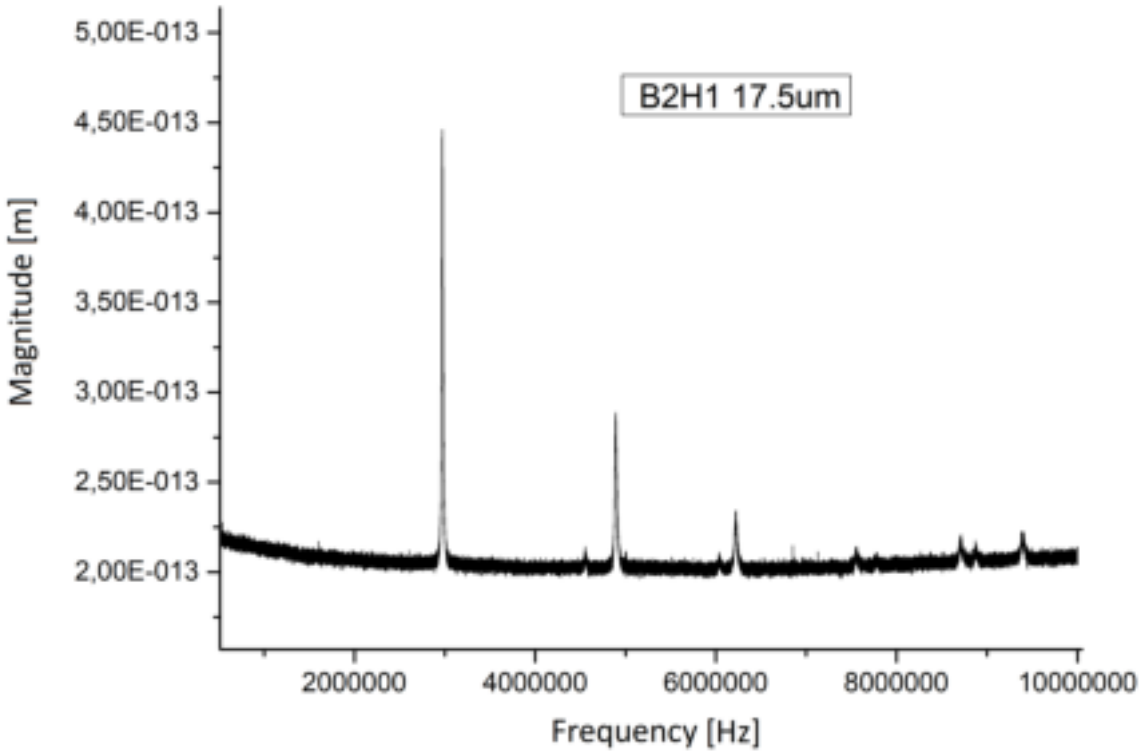

Figure 4.23: Graphene drum's spectrum

The spectrum, magnitude versus frequency, shows the mechanical vibrational behavior of the membrane under examination. As reported by the theory of the circular membrane, it vibrates in different modes which have their own frequency and magnitude. In the figure above each vibrational mode corresponds to a precise peak. The first vibrational mode corresponds to the first peak, the second vibrational mode corresponds to the second peak, etc... The modes shape of a circular membrane are represented in the following figure.
In addition, thanks to the frequency spectrum obtained, it is possible to acquire the precise value of the mode frequency and the Q factor. Both of them are obtained by using the software Origin. The experimental data are fitted through Origin using the

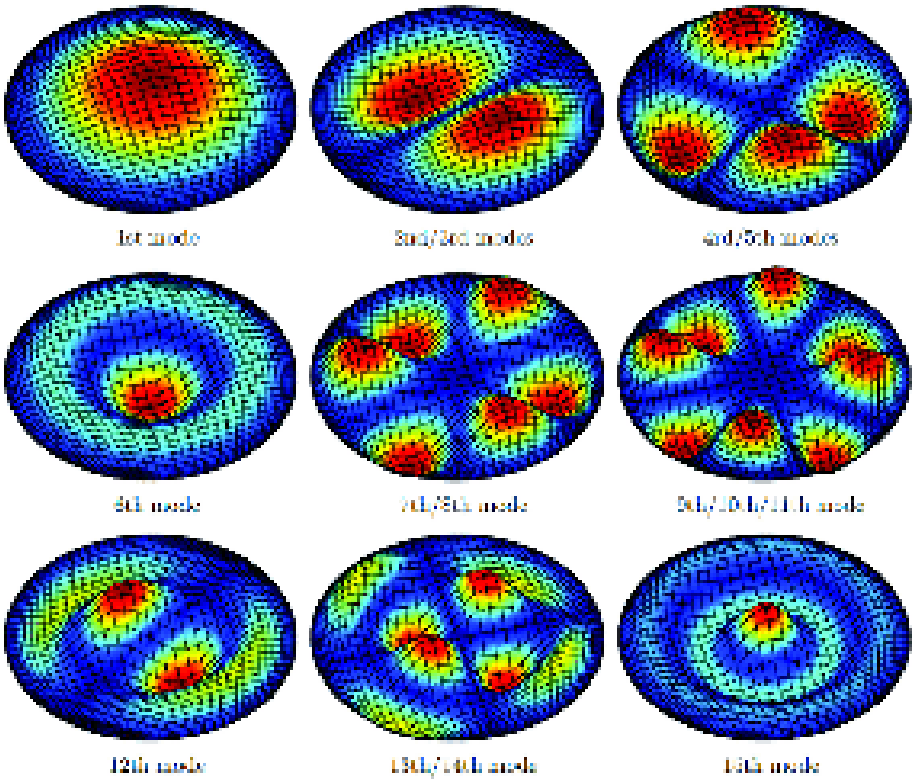

Figure 4.24: Physical representation of modes shape of a circular membrane [38]

"Non-linear curve fit tool" (Toolbar / Analysis / Non-linear curve fit). This tool allows to view the mathematical models for the fit and the possibility to edit them. The curve proposed to fit the peaks is the Lorentzian, whose equation and characteristics are :

$$y = y_0 + \frac{2A}{\pi} \frac{w}{4(x - x_c)^2 + w^2} \tag{4.1}$$

where :

- y_0 = baseline
- x_c = maximun abscissa of the curve
- A = area under the curve
- w = FWHM

While the mode frequency corresponds to the maximum abscissa obtained by the Non linear fit, the calculation of the Q factor results more complex. In fact it is necessary to perform the Non Linear Fit only after having squared-elevated the magnitude of the signal. In this way, the obtained Q factor value results more accurate. The Q factor corresponds to :

$$Q = \frac{x_c}{w} \tag{4.2}$$

an example is showed in the figure below

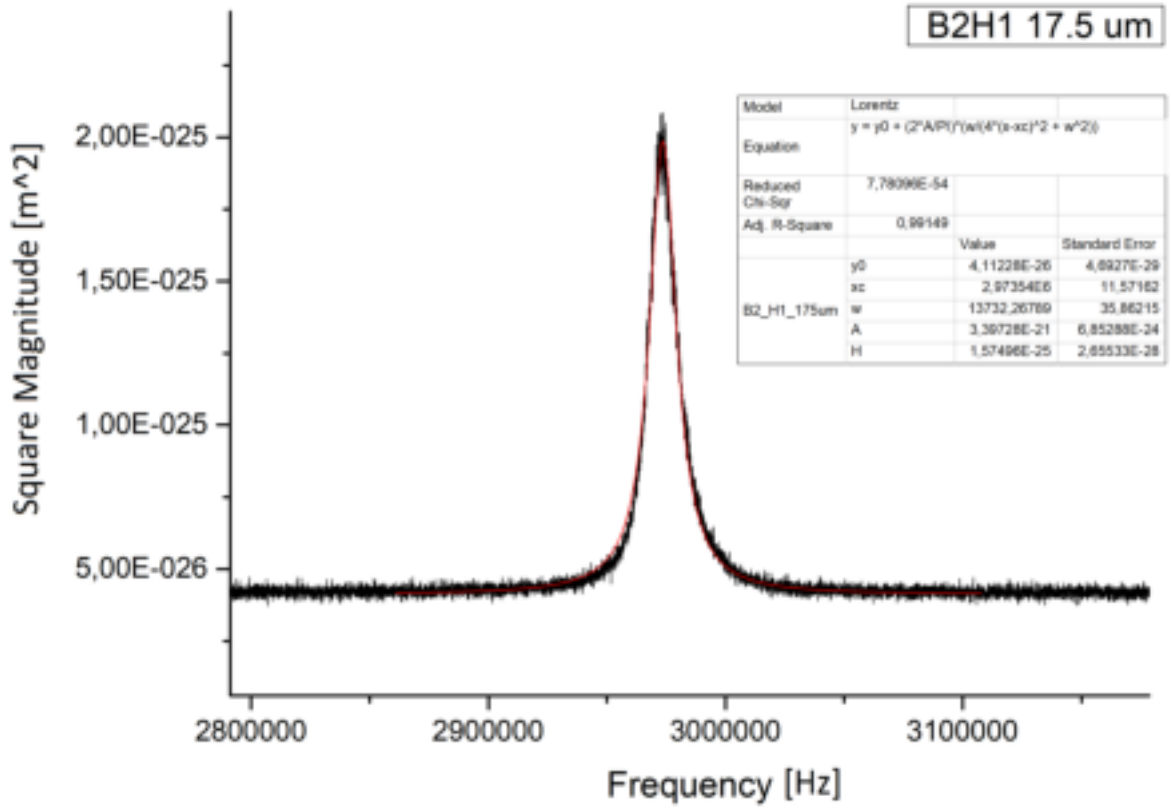

Figure 4.25: Non linear Lorentian fit of B2H1 17.5μm graphene drum

In addition, having the precise value of the first mode, one can also obtain a value of the tension that the membrane has. This is simple to obtain, in fact the tension corresponds to :

$$\sigma = \rho h \frac{R^2 f^2}{\alpha_1} \tag{4.3}$$

where

- σ is the tension
- ρ is the mass density
- h is the heigth
- R is the radius of the membrane
- f is the frequency value
- α_1 is the mode coefficient that for the first mode corresponds to 2.404

4.2.1 Characterized samples

These are the three samples which are measured and characterized : EPFL (a sample produced from EPFL), G205n and G217 (two sample produced from Politecnico di Torino). Before doing the mechanical characterization of the various membranes, it was carried out through the use of the Vibrometer in "White light Mode" and Scanning electron microscope SEM, a careful investigation into which manufactured holes were actually covered.

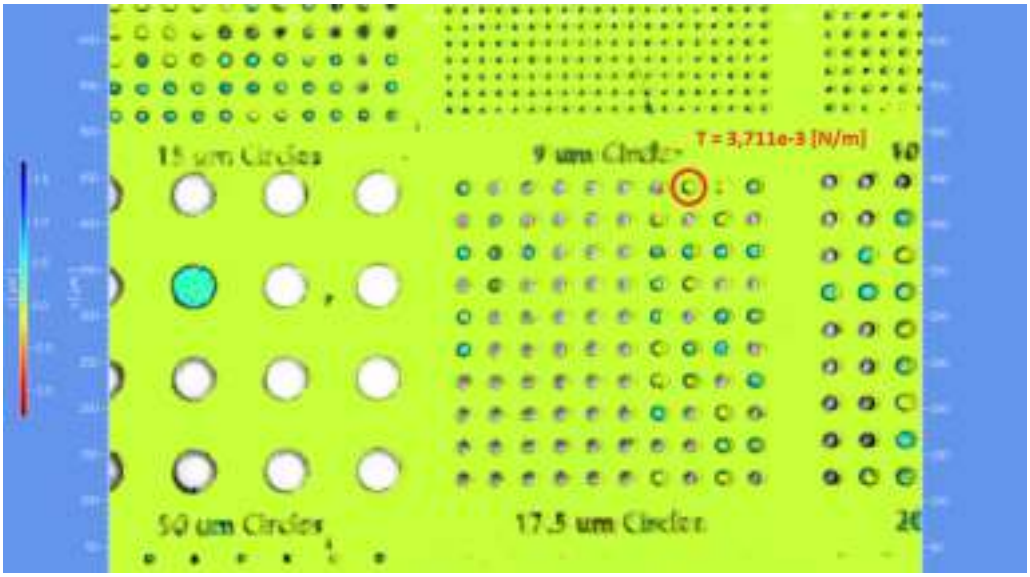

Figure 4.26: Image obtained with "White light mode" of a region with 17,5μm holes of the sample EPFL

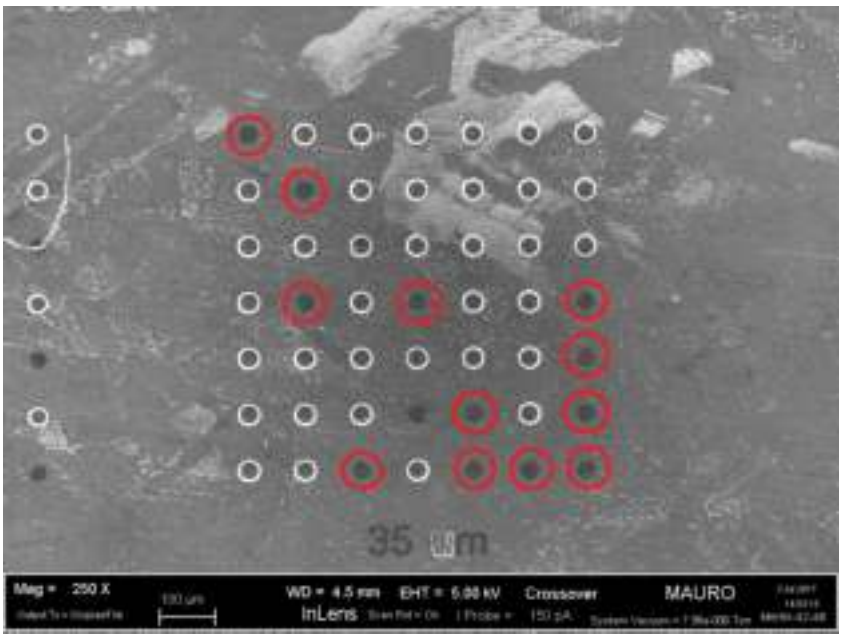

Figure 4.27: Image obtained with SEM of a region with 35μm holes of the sample G205n

The first image, obtained by using the vibrometer in "White Light Mode", shows how the covered holes have a green or blue color, while the uncovered holes have a white color. The second image was obtained by using the SEM, the holes which are covered show a darker color, while uncovered ones show a brighter edge. This is due to the fact that the graphene membranes are collapsed inside the holes. In the first image the measured membrane is circled in red, while in the second one all the membranes that have been measured in that region of circular holes with a diameter of 35 μm are circulated in red. The samples, as already explained in the previous section, have various regions with circular holes of different diameters. In order to assign a name to the measured membrane, the first part of the name corresponds to the region, while the second part corresponds to the precise position of the hole in that particular region.

EPFL sample

The obtained results are resumed in the following tabular, where the values of the first fouth modes in [Hz], the Q factor and the membrane tension in [N/m] are described.

$50\mu m$	First Mode	Second Mode	Third Mode	Fourth Mode	Qfactor	Tension
A2B2	1,60E+06	3,16E+06	3,55E+06	3,96E+06	321,9	0,0087
A1A4	1,35E+06	1,97E+06	2,20E+06	2,80E+06	147,1	0,0062
B1A4	5,52E+05	9,06E+05	9,80E+05	1117000	113,5	0,0010
B1B4	8,07E+05	1,15E+06	1,41E+06	1,53E+06	220,5	0,0022

Figure 4.28: EPFL measured graphene drums with a radius of $50\mu m$

$25\mu m$	First Mode	Second Mode	Third Mode	Fourth Mode	Qfactor	Tension
A1E7	2,41E+06	3,70E+06	5,45E+06	6,55E+06	90,2	0,0049
A1E4	2,53E+06	4,89E+06	6,35E+06	6,80E+06	131,4	0,0054
A1G6	2,21E+06	3,40E+06	3,48E+06	5,05E+06	278,3	0,0041
C3A3	3,28E+06	7,25E+06			338,7	0,0092
C3G4	2,18E+06	4,88E+06			142,1	0,0040
C3F6	2,84E+06	5,90E+06	6,40E+06	7,60E+06	113,6	0,0069
C3B3	2,57E+06	3,78E+06	5,60E+06	6,60E+06	310,5	0,0056

Figure 4.29: EPFL measured graphene drums with a radius of $25\mu m$

$20\mu m$	First Mode	Second Mode	Third Mode	Fourth Mode	Qfactor	Tension
C3G2	4,58E+06					0,0115
C3C5	4,08E+06				239,6	0,0091
C3G3	4,45E+06					0,0108
C3C7	3,64E+06	5,88E+06	6,93E+06	8,31E+06	168,2	0,0072

Figure 4.30: EPFL Measured graphene drums with a radius of $20\mu m$

$17,5\mu m$	First Mode	Second Mode	Third Mode	Fourth Mode	Qfactor	Tension
B2I8	4,35E+06	6,70E+06				0,0079
B2I1	3,00E+06	4,59E+06	4,96E+06	6,38E+06	162,2	0,0037
B2H7	4,79E+06				266,1	0,0096
B2H4	4,58E+06	6,70E+06				0,0088
B2H1	2,97E+06	4,54E+06	4,89E+06	6,03E+06	215,5	0,0037
B2G7	3,53E+06	5,78E+06	8,12E+06		181,8	0,0052
B2G2	2,88E+06	3,60E+06	5,70E+06			0,0034

Figure 4.31: EPFL measured graphene drums with a radius of $17,5\mu m$

$15\mu m$	First Mode	Second Mode	Third Mode	Fourth Mode	Qfactor	Tension
B2N8	4,51E+06	5,84E+06	7,28E+06	7,56E+06	219,3	0,0062
B2N10	4,48E+06	5,83E+06	7,24E+06	7,51E+06	336,15	0,0062
B2N6	3,53E+06	5,20E+06	7,67E+06	8,48E+06		0,0038
B2B11	2,17E+06	3,23E+06	3,66E+06	4,22E+06	94,1	0,0014
B2B9	4,45E+06					0,0061
B2N3	4,06E+06	6,47E+06	9,34E+06			0,0050
C3F4	4,03E+06	6,61E+06	7,91E+06	8,51E+06	193,1	0,0050

Figure 4.32: EPFL measured graphene drums with a radius of $15\mu m$

$10\mu m$	First Mode	Second Mode	Third Mode	Fourth Mode	Qfactor	Tension
C3N10	5,88E+06	1,05E+07			112,4	0,0047
C3N9	5,60E+06	7,51E+06	9,40E+06	1,03E+07		0,0043
C3I10	5,46E+06	9,45E+06	1,15E+07	1,19E+07	88,9	0,0041
C3H9	6,09E+06	9,52E+06	1,03E+07	1,25E+07	92,68	0,0050
C3H10	5,84E+06	1,25E+07	1,34E+07	1,86E+07	87,6	0,0046
C3H8	6,34E+06	1,03E+07	1,54E+07		219,1	0,0055
C3H7	6,70E+06	1,38E+07				0,0061
C3Q2	4,77E+06	7,23E+06	1,00E+07	1,36E+07		0,0031
C3P2	7,04E+06	1,12E+07			214,1	0,0068
C3R1	5,90E+06	9,22E+06	1,26E+07			0,0047
C3H6	5,96E+06	9,88E+06	1,16E+06	1,63E+07	103	0,0048

Figure 4.33: EPFL measured graphene drums with a radius of $10\mu m$

$9\mu m$	First Mode	Second Mode	Third Mode	Fourth Mode	Qfactor	Tension
C3N9	1,01E+07	1,17E+07	1,58E+07	1,68E+07		0,0113
C3L9	7,80E+06	1,58E+07			67,5	0,0067
C3L8	8,48E+06	1,09E+07	1,97E+07		82,1	0,0080
C3L7	7,02E+06	1,12E+07	1,41E+07			0,0054
C3I9	8,14E+06	1,53E+07			83,9	0,0073
C3I7	8,37E+06	1,75E+07	1,92E+07		121,1	0,0077
C3H7	8,17E+06	1,18E+07	1,34E+07	1,60E+07	87,8	0,0074
C3N7	8,40E+06	1,25E+08	1,78E+07			0,0078

Figure 4.34: EPFL measured graphene drums with a radius of $9\mu m$

$6\mu m$	First Mode	Second Mode	Third Mode	Fourth Mode	Qfactor	Tension
C3L11	7,53E+06	1,17E+07	1,72E+07		128,3	0,0028
C3L8	9,23E+06				79,5	0,0042
C3I8	9,30E+06	1,94E+07			86,5	0,0042
C3L10	8,07E+06	1,46E+07				0,0032
C3I10	7,90E+06	1,13E+07	1,65E+07			0,0030
C3D14	9,05E+06	1,69E+07	1,78E+07		99,1	0,0040
C3L9	6,23E+06	9,19E+06	1,39E+07			0,0019
C3I9	9,31E+06				84,8	0,0042
C3D13	7,34E+06					0,0026
C3D12	1,14E+07					0,0064
C3H6	7,46E+06	1,17E+07	1,46E+07		95,8	0,0027
C3H8	1,04E+07	1,18E+07	1,44E+07	1,91E+07		0,0053

Figure 4.35: EPFL measured graphene drums with a radius of $6\mu m$

$5\mu m$	First Mode	Second Mode	Third Mode	Fourth Mode	Qfactor	Tension
C3R7	1,12E+07					0,0043
C3L9	1,35E+07					0,0062
C3Q7	9,68E+06				108,36	0,0032
C3L8	1,30E+07					0,0058
C3N7	1,42E+07					0,0068
C3I10	8,00E+06					0,0021
C3L10	1,06E+07	1,48E+07	1,98E+07		109,2	0,0038
C3H10	9,38E+06					0,0030
C3D10	8,65E+06	1,47E+07	1,83E+07		66,2	0,0025
C3R3	1,19E+07	1,92E+07			142,2	0,0048
C3T2	1,24E+07	1,58E+07				0,0052
C3B13	8,66E+06	1,27E+07	1,69E+07	1,90E+07		0,0025
C3A14	8,84E+06	1,70E+07	1,85E+07		94,8	0,0026

Figure 4.36: EPFL measured graphene drums with a radius of $5\mu m$

$4\mu m$	First Mode	Second Mode	Third Mode	Fourth Mode	Qfactor	Tension
C3F12	1,36E+07					0,0040
B2Q7	1,48E+07				131,4	0,0048
C3H10	1,41E+07					0,0043
B2F6	7,34E+06	1,02E+07			14,7	0,0011
B2R8	1,10E+07	1,61E+07				0,0026

Figure 4.37: EPFL measured graphene drums with a radius of $4\mu m$

$3\mu m$	First Mode	Second Mode	Third Mode	Fourth Mode	Qfactor	Tension
C3H8	1,21E+07				64,9	0,0018
C3M12	1,35E+07				127,7	0,0022
C3L7	1,31E+07				49,7	0,0021

Figure 4.38: EPFL measured graphene drums with a radius of $3\mu m$

G205n sample

The obtained results are resumed in the following tabular, where the values of the first fouth modes in [Hz], the Q factor and the membrane tension in [N/m] are described.

$55\mu m$	First Mode	Second Mode	Third Mode	Fourth Mode	Qfactor	Tension
B1C5	7,30E+05	1,55E+06			289,1	0,0021
B2C3	1,02E+06	1,48E+06	1,62E+06			0,0041
B1E1	6,02E+05	8,66E+05	9,20E+05	1,12E+06	476,2	0,0014

Figure 4.39: G205 measured graphene drums with a radius of $50\mu m$

$50\mu m$	First Mode	Second Mode	Third Mode	Fourth Mode	Qfactor	Tension
B1C5	6,32E+05	9,83E+05	1,07E+06	1,32E+06		0,0013
A2D2	1,02E+06	2,27E+06			466,1	0,0003
A2A2	1,06E+06					0,0003

Figure 4.40: G205 measured graphene drums with a radius of $45\mu m$

$45\mu m$	First Mode	Second Mode	Third Mode	Fourth Mode	Qfactor	Tension
B2E5	1,38E+06	1,97E+06	246,1	0,0051		
B2B5	9,65E+05	1,49E+06	1,68E+06	1,78E+06	118,3	0,0025
B1E5	8,78E+05	1,26E+06	1,40E+06	1,58E+06		0,0021
B1E3	7,04E+05	1,15E+06	1,30E+06	1,48E+06		0,0013
B1D5	7,94E+05	1,13E+06	1,25E+06	1,48E+06	402,1	0,0017
B1D4	7,70E+05	1,25E+06	1,43E+06	1,73E+06	149,2	0,0016
B1D3	7,35E+05	1,04E+06	1,34E+06	1,59E+06	162,3	0,0014
B1C5	7,47E+05	1,19E+06	1,26E+06	1,61E+06	141,9	0,0015
B1B5	8,13E+05	1,20E+06	1,37E+06	1,56E+06	293,4	0,0017
A2E3	1,16E+06	2,01E+06	2,47E+06	2,87E+06		0,0036
A2D3	1,09E+06	1,76E+06	2,47E+06	4,14E+06	167,2	0,0032
A2C5	9,78E+05	1,39E+06	1,86E+06	2,06E+06	241,1	0,0025
A2C4	1,01E+06	1,63E+06	1,97E+06	2,90E+06		0,0027
A2A2	1,08E+06	1,50E+06	1,58E+06	2,17E+06		0,0031
A2A1	8,99E+05	1,63E+06	1,92E+06	3,06E+06	98,4	0,0022

Figure 4.41: G205 easured graphene drums with a radius of $40\mu m$

$40\mu m$	First Mode	Second Mode	Third Mode	Fourth Mode	Qfactor	Tension
B2G6	1,00E+06	1,55E+06	1,76E+06	2,91E+06	300,8	0,0021
B2G7	9,70E+05	1,36E+06	1,60E+06	1,89E+06		0,0020
B2G5	9,03E+05	1,33E+06	1,75E+06	1,86E+06	194,6	0,0017
B2G4	9,15E+08	1,37E+06	1,44E+06	1,83E+06	187,7	0,0018
B2F7	8,03E+05	1,59E+06	1,65E+06	1,85E+06	337,9	0,0014
B2E7	8,13E+05	1,85E+06	1,98E+06	2,68E+06	305,8	0,0014
B2E6	8,48E+05	1,31E+06	2,16E+06	2,33E+06	221,7	0,0015
B2D4	7,37E+05	1,00E+06	1,25E+06	1,56E+06	314,9	0,0011
B2C7	8,57E+05	1,22E+06	1,30E+06	1,66E+06	237,2	0,0015
B2B2	8,98E+05	1,24E+06	1,68E+06	1,83E+06	169,5	0,0017
B2A1	1,02E+06	1,69E+06	3,21E+06			0,0022
A2F4	1,77E+06	2,91E+06	5,06E+06	5,62E+06		0,0065

Figure 4.42: G205 easured graphene drums with a radius of $35\mu m$

$35\mu m$	First Mode	Second Mode	Third Mode	Fourth Mode	Qfactor	Tension
B2G5	1,16E+06	2,74E+06				0,0022
B2F3	1,11E+06	1,61E+06	2,03E+06	3,14E+06	183,5	0,0020
B2E5	1,05E+06	1,47E+06	1,73E+06	1,94E+06	2,00E+02	0,0018
B2E4	8,37E+05	1,17E+06	1,40E+06	1,74E+06	165,6	0,0011
B2C5	9,02E+05	1,26E+06	1,82E+06	1,94E+06	163,8	0,0013
B2C4	1,08E+06	1,49E+06	1,71E+06	2,00E+06		0,0019
B2B6	1,11E+06	1,76E+06	1,98E+06	2,28E+06	263,1	0,0020
B2B4	1,09E+06	1,57E+06	1,93E+06	2,20E+06	156,7	0,0019
A2G2	1,75E+06	4,01E+06			255,6	0,0049
A2F4	1,77E+06	2,91E+06	5,06E+06	5,62E+06		0,0050
A2B4	1,61E+06	3,19E+06	4,80E+06		160,5	0,0042
A2A5	2,39E+06				170,3	0,0092
A2A4	1,51E+06	2,25E+06	2,68E+06	3,33E+06	144,6	0,0036

Figure 4.43: G205 measured graphene drums with a radius of $30\mu m$

$30\mu m$	First Mode	Second Mode	Third Mode	Fourth Mode	Qfactor	Tension
B2B5	1,24E+06	1,90E+06	2,08E+06	2,69E+06	10,22086562	0,0018
B2A7	1,48E+06	2,28E+06	2,94E+06	3,19E+06	277,2353161	0,0026
B2A5	9,88E+05	1,44E+06	1,62E+06	2,04E+06	97,57865113	0,0012
A2G3	1,82E+06	2,51E+06	3,11E+06	3,46E+06	184,824508	0,0039
A2F1	1,62E+06	2,34E+06	2,76E+06	3,28E+06	167,0114943	0,0031
A2D6	1,65E+06	2,54E+06	3,33E+06	3,86E+06	252,364968	0,0032
A2A1	1,81E+06	2,47E+06	2,72E+06	3,10E+06	206,3133903	0,0039

Figure 4.44: G205 measured graphene drums with a radius of $25\mu m$

$25\mu m$	First Mode	Second Mode	Third Mode	Fourth Mode	Qfactor	Tension
A2E9	1,44E+06	1,83E+06	2,52E+06	3,29E+06	89,7	0,0017
A2D9	1,71E+06	2,98E+06	4,12E+06		110,8	0,0024
A2B6	1,98E+06	2,50E+06	3,08E+06		85,6	0,0032
A2B4	1,70E+06	2,32E+06	2,73E+06	3,15E+06	1,57E+02	0,0023
A2A4	1,29E+06	1,96E+06	2,48E+06	3,08E+06	205,5	0,0014
A2A3	2,12E+06	3,54E+06	4,84E+06	5,35E+06	137,7	0,0036
A2A2	1,47E+06	3,28E+06			81,9	0,0017
A2A1	2,37E+06	3,26E+06	4,63E+06			0,0046

Figure 4.45: G205 measured graphene drums with a radius of $20\mu m$

$20\mu m$	First Mode	Second Mode	Third Mode	Fourth Mode	Qfactor	Tension
B2G7	1,90E+06	2,48E+06	3,15E+06	3,57E+06	130,1	0,0019
A2B8	3,27E+06	4,11E+06	4,66E+06	5,59E+06		0,0056

Figure 4.46: G205 measured graphene drums with a radius of $15\mu m$

$15\mu m$	First Mode	Second Mode	Third Mode	Fourth Mode	Qfactor	Tension
B2L9	2,09E+06	3,10E+06	4,46E+06	4,92E+06		0,0013
B2L7	2,24E+06	3,70E+06	5,38E+06	7,38E+06	109,6	0,0015
B2I7	2,54E+06	4,19E+06	5,96E+06	6,51E+06	119,9	0,0019
A2F4	3,65E+06	5,93E+06	7,23E+06	8,59E+06		0,0039
A2E4	3,67E+06	4,79E+06				0,0040
A2D5	4,28E+00	5,54E+06			124,9	0,0054
A2C5	5,19E+06					0,0080
A2C4	3,22E+06	4,27E+06	7,69E+06	9,14E+06	120,6	0,0031

Figure 4.47: G205 measured graphene drums with a radius of $10\mu m$

$10\mu m$	First Mode	Second Mode	Third Mode	Fourth Mode	Qfactor	Tension
B2C4	3,13E+06	7,59E+06	9,60E+06	1,14E+07		0,0013
B2B4	5,41E+06	7,66E+06	9,81E+06	1,19E+07		0,0038
B2A8	4,14E+06	5,15E+06	7,28E+06	1,28E+07	121,5	0,0023
B2A7	8,06E+06					0,0085
A2C4	9,13E+05				52,2	0,0001
A2B3	5,46E+06	8,82E+06	1,15E+07	1,38E+07		0,0039
A2B3	6,42E+06	8,91E+06	9,99E+06	1,11E+08	131,8	0,0054
A2A3	4,42E+06	6,39E+06	7,38E+06	8,53E+06	89,9	0,0026
A2A2	8,88E+06					0,0104

Figure 4.48: G205 measured graphene drums with a radius of $5\mu m$

G217

The obtained results are resumed in the following tabular, where the values of the first fouth modes in [Hz], the Q factor and the membrane tension in [N/m] are described.

$50\mu m$	First Mode	Second Mode	Third Mode	Fourth Mode	Qfactor	Tension
C3A1	1,59E+06	2,26E+06	3,10E+06	3,51E+06	9,14+02	0,008

Figure 4.49: G217 measured graphene drums with a radius of $50\mu m$

$40\mu m$	First Mode	Second Mode	Third Mode	Fourth Mode	Qfactor	Tension
C3B3	2,07E+06	3,06E+06	3,20E+06	3,52E+06	524	0,008
C3A3	1,64E+06	2,55E+06	3,15E+06	3,51E+06		0,007

Figure 4.50: G217easured graphene drums with a radius of $40\mu m$

$20\mu m$	First Mode	Second Mode	Third Mode	Fourth Mode	Qfactor	Tension
C3E5	2,31E+06	3,35E+06	4,46E+06	4,60E+06		0,002
C3B4	1,82E+06	2,66E+06	2,96E+06	3,61E+06	1,51E+03	0,001
C3B3	1,94E+06	2,84E+06	3,30E+06	4,05E+06		0,002
C3A2	2,76E+06	3,85E+06	4,63E+06	5,20E+06		0,003

Figure 4.51: G217 measured graphene drums with a radius of $20\mu m$

$10\mu m$	First Mode	Second Mode	Third Mode	Fourth Mode	Qfactor	Tension
C3A1	2,43E+06	3,69E+06	5,00E+06	8,87E+06		0,0008

Figure 4.52: G217 measured graphene drums with a radius of $10\mu m$

Chapter 5

Discussion of results

In order to obtain a great comparison between the samples characterized, it was decided to study their average behavior. Given the high number of membranes which have been measured, this was made on the EPFL sample and on the G205n sample. This type of study leads to obtain the average values of the first measured modes, deriving their standard deviation and representing them according to the diameter of the membranes. Furthermore, since all the membranes are tensioned, an average tension has been obtained and it corresponds to : σ_{EPFL}=0.005 [N/m] for the EPFL sample and σ_{G205n}=0.003[N/m] for G205n. In the two graphs below, the average trends of the first modes in respect to the diameter of the circular membranes are then reported for each sample. In addition, using the average tension values obtained, it was possible to calculate the frequency of the first mode for each radius by using

$$\Omega_{1,i} = \frac{2.404}{R_i}\sqrt{\frac{\sigma_{Average}}{\rho h}} \tag{5.1}$$

where $\Omega_{1,i}$ is the first mode corresponding to the radius i, R_i is the i radius , 2.404 corresponds to the coefficient proper of first mode, ρ is the mass density of graphene, h is the height and $\sigma_{Average}$ correspond to the average tension of the sample. Thanks to this calculation it was possible to obtain the best fit of the experimental data. This is represented in green in the following graphs. As can be seen in both cases, EPFL and G205n samples, the trend results to be proportional to 1/R, as predicted by circular membrane theory. Membranes with a short diameter have an higher frequency in respect to those with a larger diameter. In addition, the two samples show average tensions that appear to have the same order of magnitude. This leads to note that the two measured samples, EPFL and G205n, report very similar frequency behaviors.

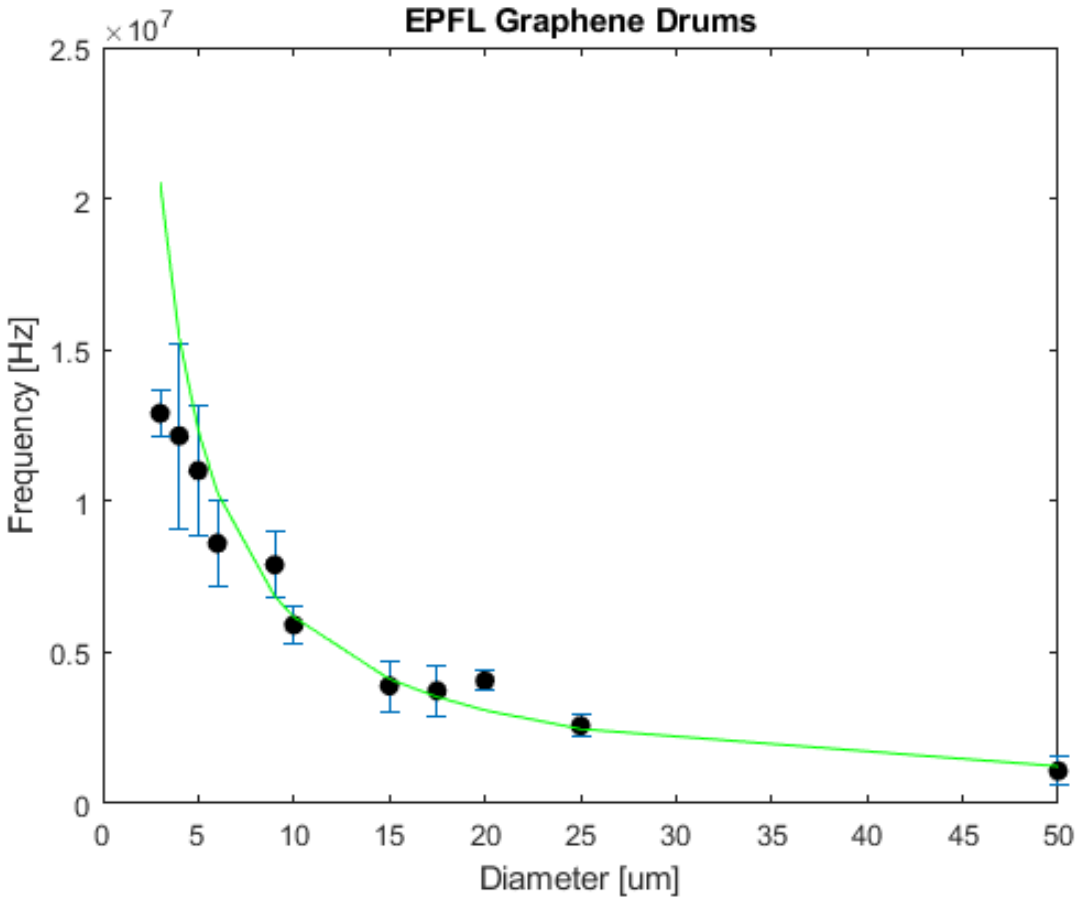

Figure 5.1: Average frequency with standard deviation vs diameter of the EPFL sample

Diameter μm	Average First Mode	Dev.St
50	1,08E+06	4,82E+05
25	2,57E+06	3,82E+05
20	4,06E+06	3,32E+05
17,5	3,73E+06	8,27E+05
15	3,89E+06	8,35E+05
10	5,91E+06	5,92E+05
9	7,89E+06	1,10E+06
6	8,60E+06	1,45E+06
5	1,10E+07	2,17E+06
4	1,22E+07	3,06E+06
3	1,29E+07	7,30E+05

Figure 5.2: Average frequency values with standard deviation of EPFL sample

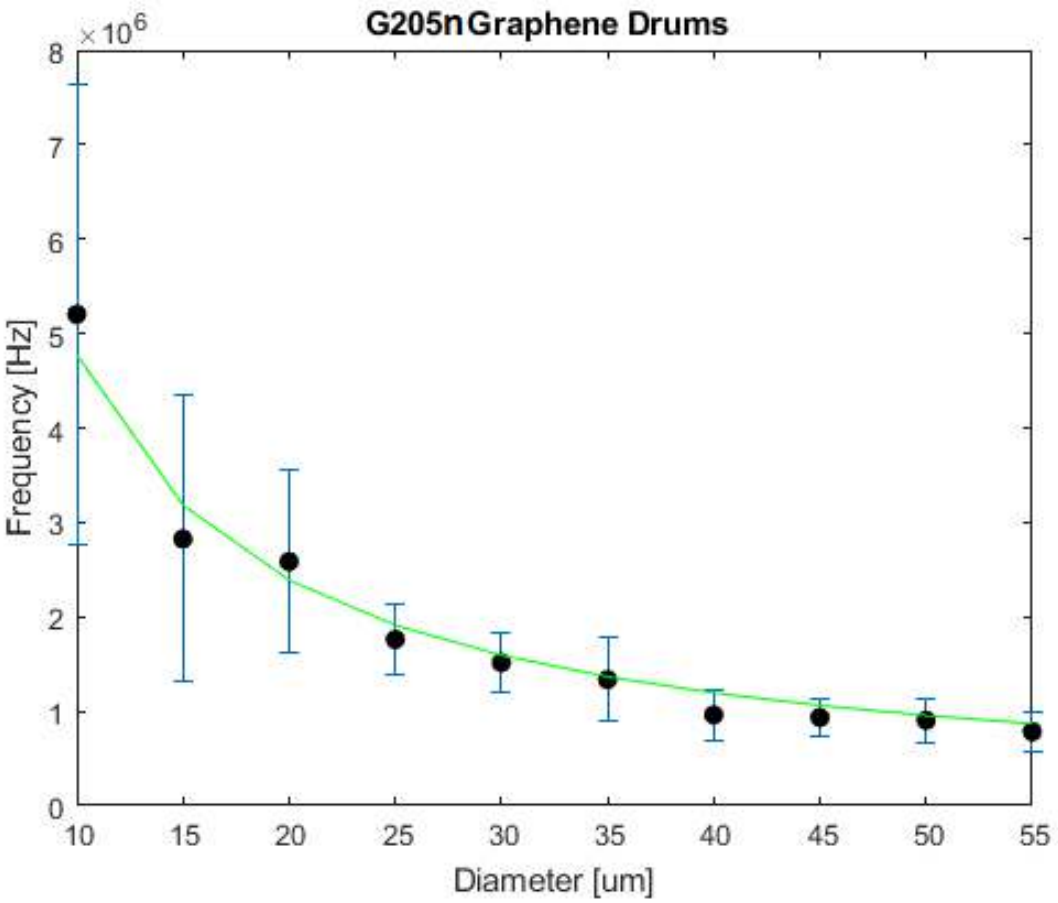

Figure 5.3: Average frequency with standard deviation vs diameter of the G205 sample

Diameter μm	Average First Mode	Dev.St
55	7,84E+5	2,14E+5
50	9,04E+5	2,36E+5
45	9,33E+5	1,88E+5
40	9,61E+5	2,68E+5
35	1,34E+6	4,43E+5
30	1,52E+6	3,06E+5
25	1,76E+6	3,70E+5
20	2,58E+6	9,69E+5
15	2,83E+6	1,52E+6
10	5,20E+6	2,44E+6

Figure 5.4: Average frequency values with standard deviation of G205n sample

The same study has been done for the Q Factor. As clearly evident, the average Q factors for both samples do not follow a particular trend, but its values in both samples are reduced as the diameter decreases. This is due to the difficulty in obtaining a clear signal from the measure obtained by using the Vibrometer for membrane with a short radius and it also becomes more difficult to make a good Non linear Lorentian fit by using Origin. In addition, the average Q factor values obtained, for both samples, have the same order of magnitude.

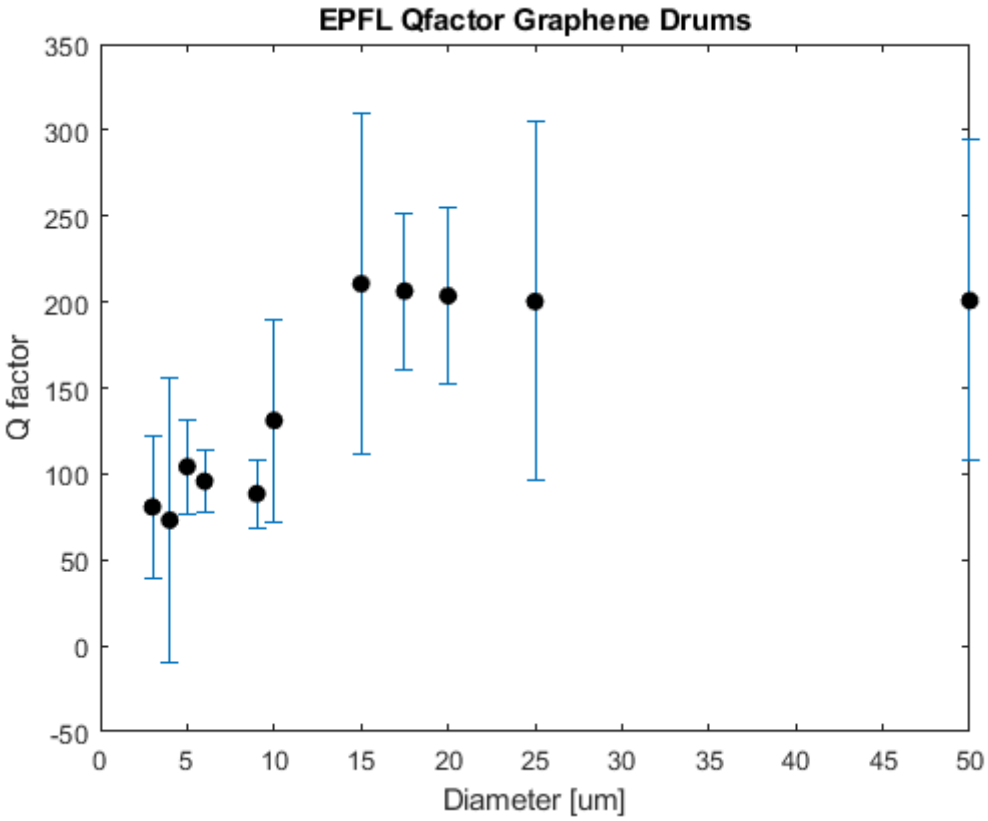

Figure 5.5: Average Q factor with standard deviation vs diameter of the EPFL sample

Diameter μm	Q factor	Dev.St
50	200,8	93,3
25	200,3	104,3
20	203,6	51
17,5	206,4	45,4
15	210,6	99,5
10	131,1	58,8
9	88,5	19,8
6	95,7	17,6
5	104,2	27,5
4	73,1	82,5
3	80,8	41,3

Figure 5.6: Average Q factor values with standard deviation of EPFL sample

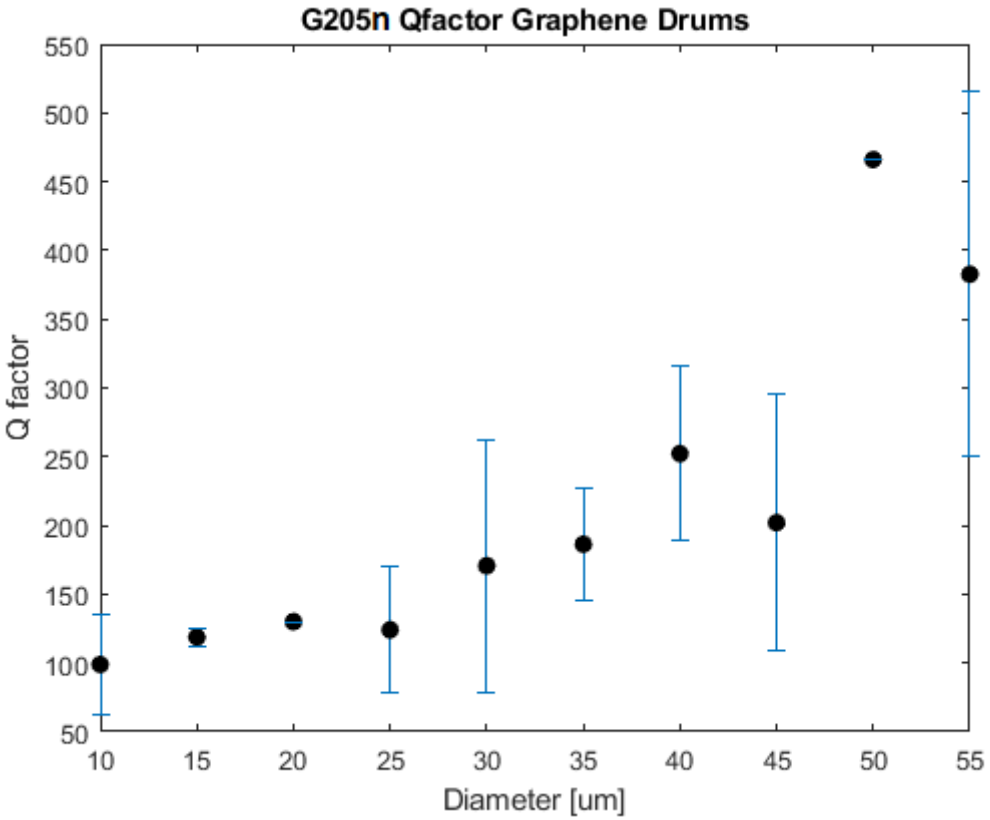

Figure 5.7: Average Q factor with standard deviation vs diameter of the G205n sample

Diameter μm	Q factor	Dev.St
55	382,6	132,3
50	466,1	0
45	202,1	93,6
40	252,3	63,2
35	186,3	41,3
30	170,8	91,8
25	124,3	45,7
20	130,1	0
15	118,8	6,5
10	98,9	35,9

Figure 5.8: Average Q factor values with standard deviation of G205n sample

5.1 Splitting of the modes

This type of average analysis was carried out by collecting the values reported by the first vibrational mode for each samples. The reason is that most of the measured graphene membranes report the phenomenon of splitting modes, as shown in [27]. This splitting of modes, as described in the previous section, strictly depends on the presence of cracks in the membrane and it is due to a symmetry breaking of the circular membrane. As reported in the figure below, there are six cases in which the phenomenon of mode splitting appear. In order to highlight this phenomenon, the frequencies which the modes should have without the split are calculated. Due to the circular membrane theory, the modes are calculated as follows :

$$\Omega_i = \frac{\alpha_i}{\alpha_1}\Omega_1 \tag{5.2}$$

where Ω_i corresponds to the frquency of the i mode, α_i is the specific coefficient of mode i, α_1 corresponds to the coefficient related to the first mode and Ω_1 is the frequency of the first mode. The coefficients values of the first three modes correspond to $\alpha_1 = 2.404$, $\alpha_2 = 3.832$ and $\alpha_3 = 5.135$. In the following spectrum the position of the second and the third mode calculated by using the theory are represented in blue line.

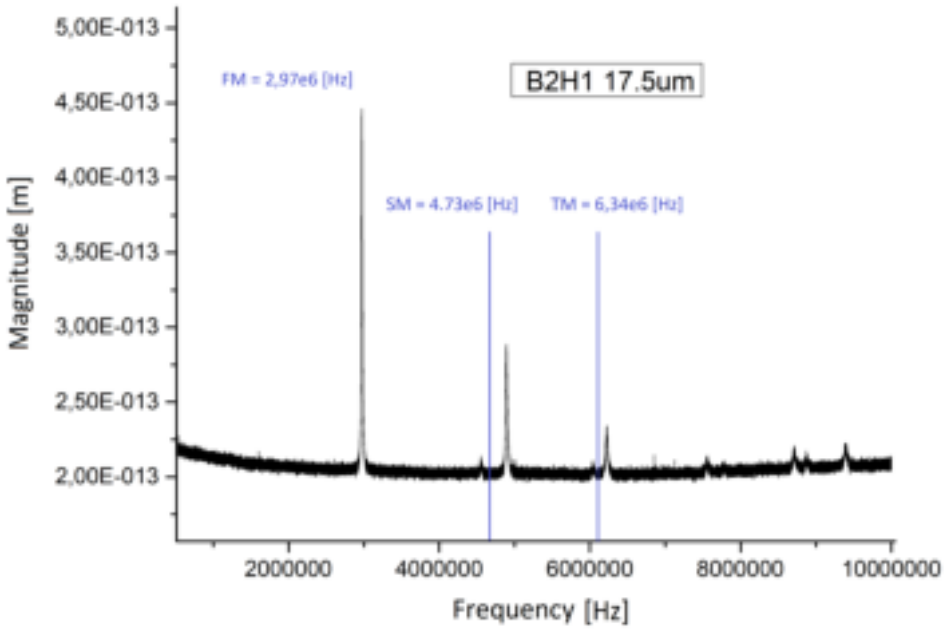

Figure 5.9: Frequency spectrum of B2H1 membrane, the blue lines corresponds to the position of the theoretical values of the second and third modes

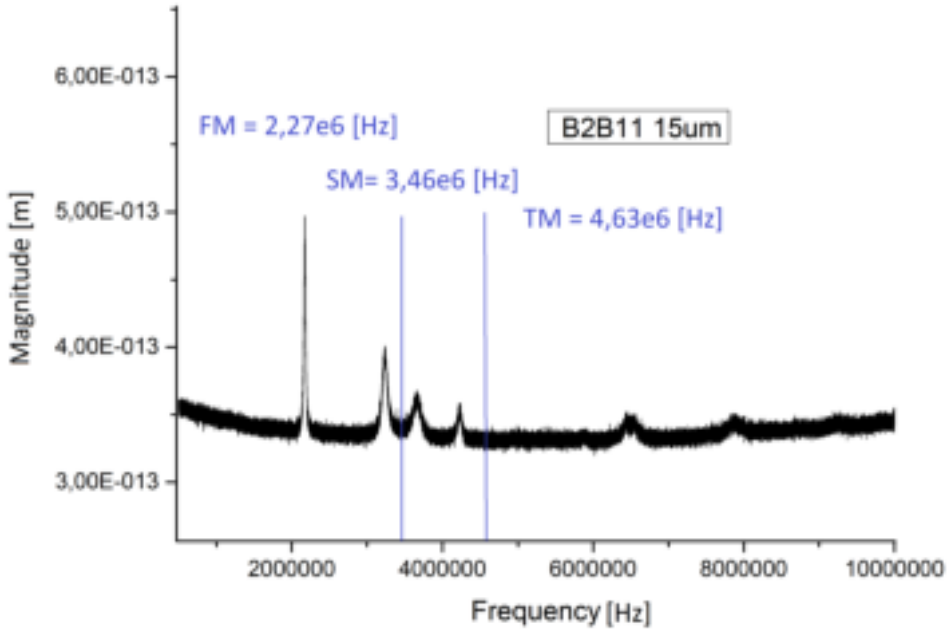

Figure 5.10: Frequency spectrum of B2B11 membrane, the blue lines corresponds to the position of the theoretical values of the second and third modes

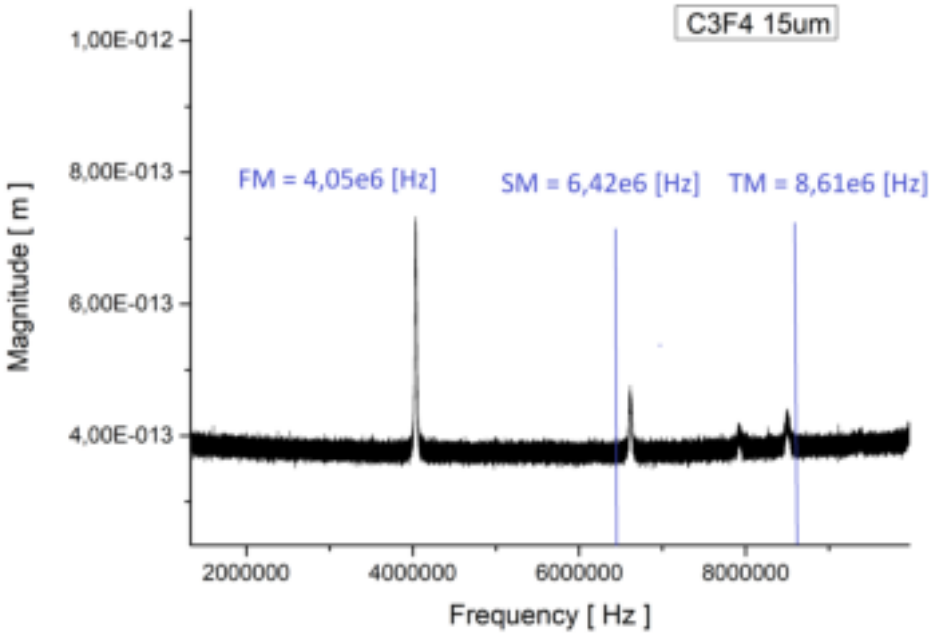

Figure 5.11: Frequency spectrum of C3F4 membrane, the blue lines corresponds to the position of the theoretical values of the second and third modes

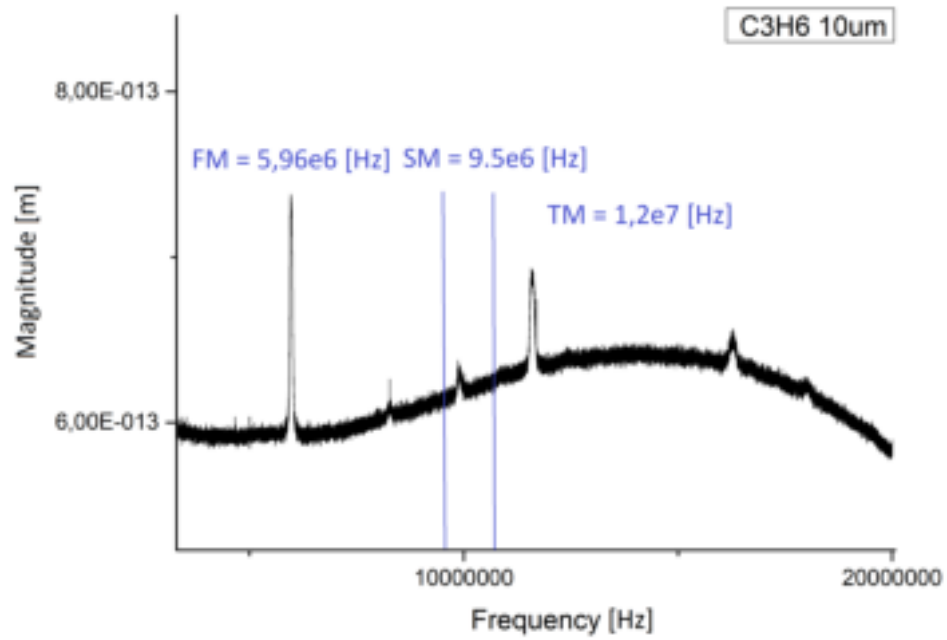

Figure 5.12: Frequency spectrum of C3H6 membrane, the blue lines corresponds to the position of the theoretical values of the second and third modes

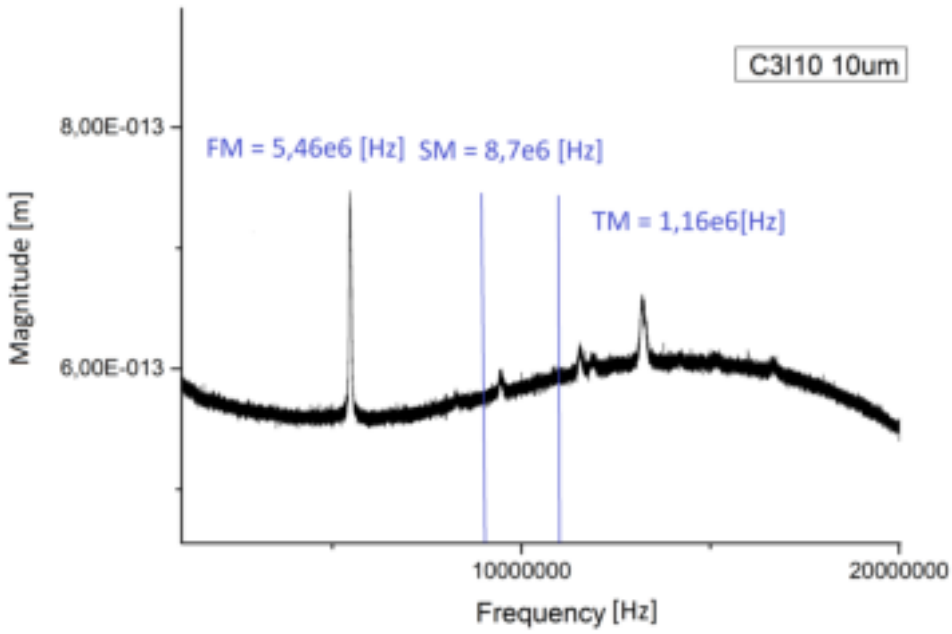

Figure 5.13: Frequency spectrum of C3I10 membrane, the blue lines corresponds to the position of the theoretical values of the second and third modes

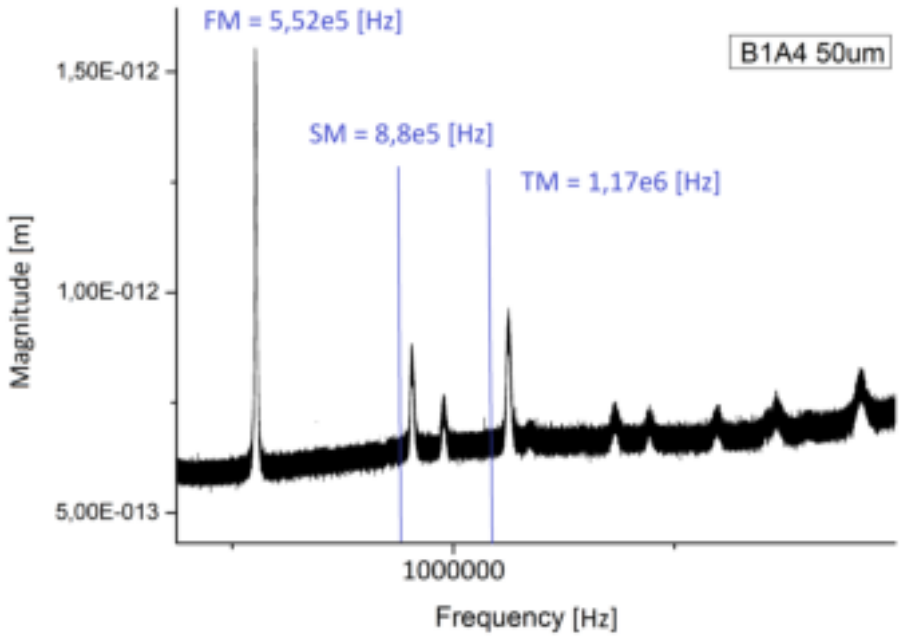

Figure 5.14: Frequency spectrum of B1A4 membrane, the blue lines corresponds to the position of the theoretical values of the second and third modes

Using Comsol it is also possible make an accurate simulation, due to a simpler geometry shape of the membrane B1A4 of the EPFL sample, one obtains the mode shape and the eigenfrequencies of the membrane. Thanks to an objective comparison between the experimental values and the simulated ones, it was possible to verify that the data reported by the simulation reflect the real ones except for small differences due to the imperfect geometrical accuracy of the membrane shape created for the simulation. Firstly the membrane shape is represented via SEM, secondly the simulated results obtained by Comsol. The results are reported in the following tabular where the eigenfrequencies are in units of [Hz].

$50\mu m$	First Mode	Second Mode	Third Mode	Fourth Mode
B1A4 experimental	5,52E+05	9,06E+05	9,80E+05	1,12E+06
B1A4 simulated	5,00E+05	9,44E+05	1,17E+06	1,69E+06

Figure 5.15: EPFL B1A4 graphene membrane with a diameter of $50\mu m$

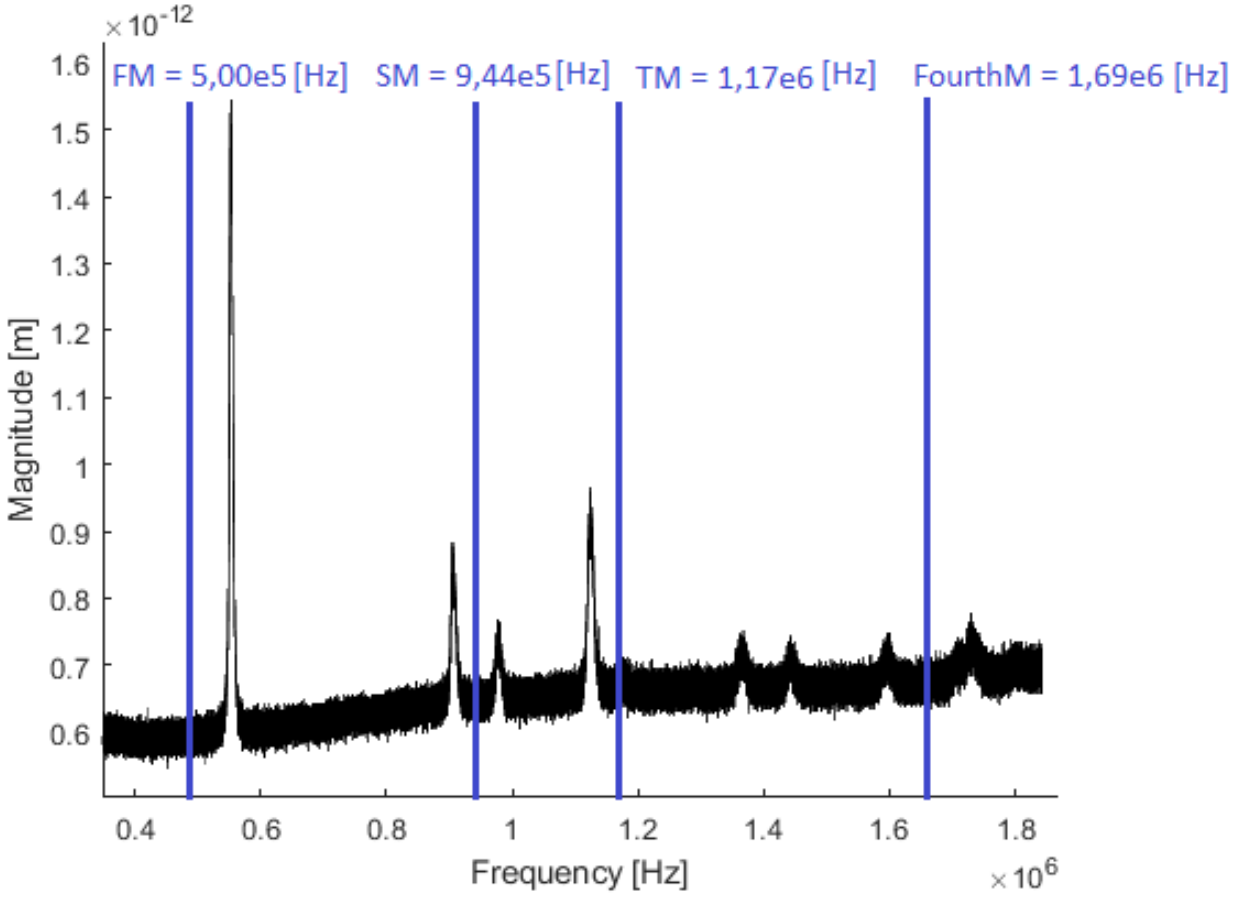

Figure 5.16: Frequency spectrum of B1A4 membrane, the blue lines corresponds to the position of the simulation values of the first four modes

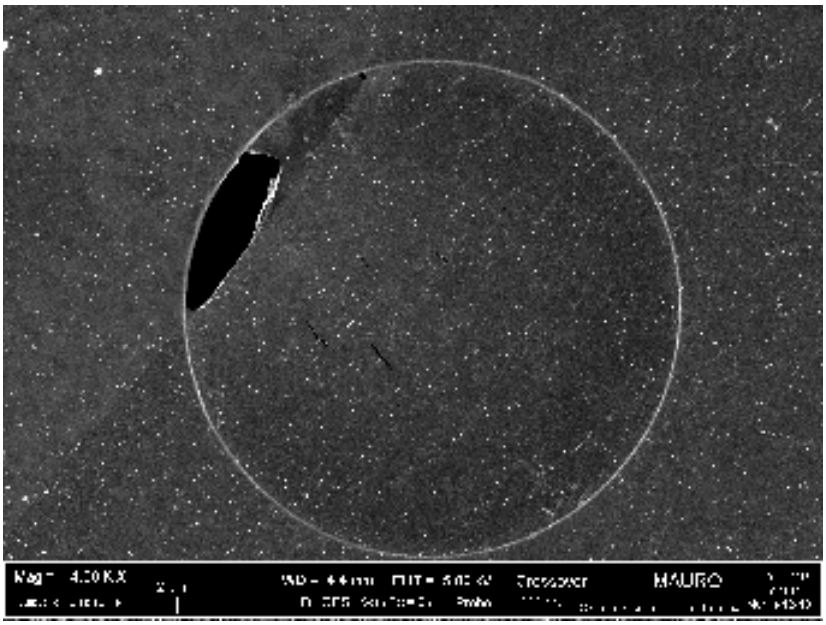

Figure 5.17: Image obtained with SEM of B1A4 membrane with $50\mu m$ of diameter

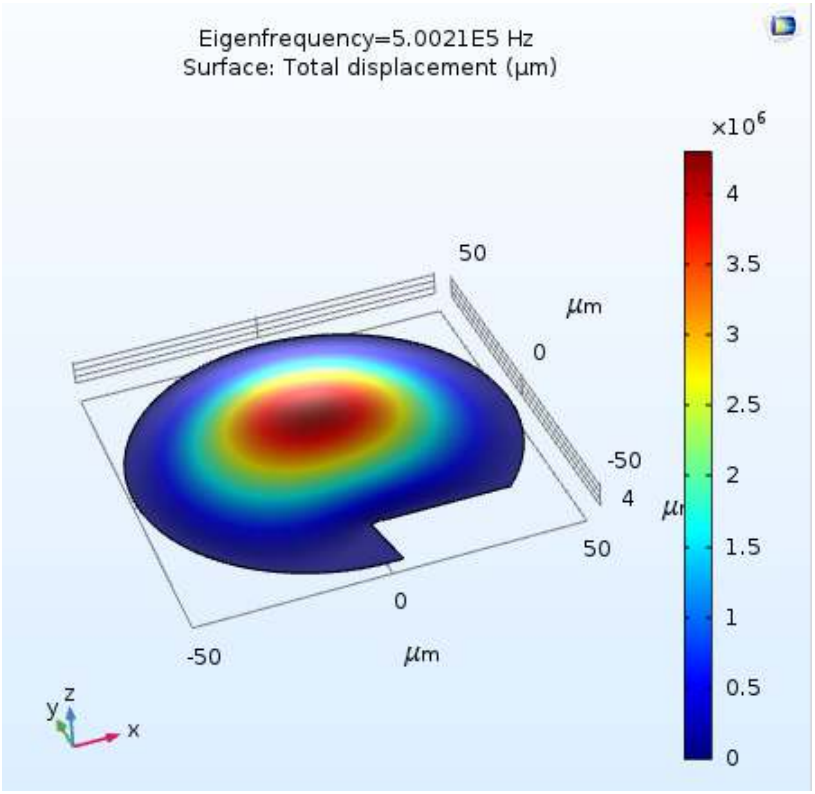

Figure 5.18: Mode shape and eigenfrequency of the first vibrational mode of B1A4 membrane

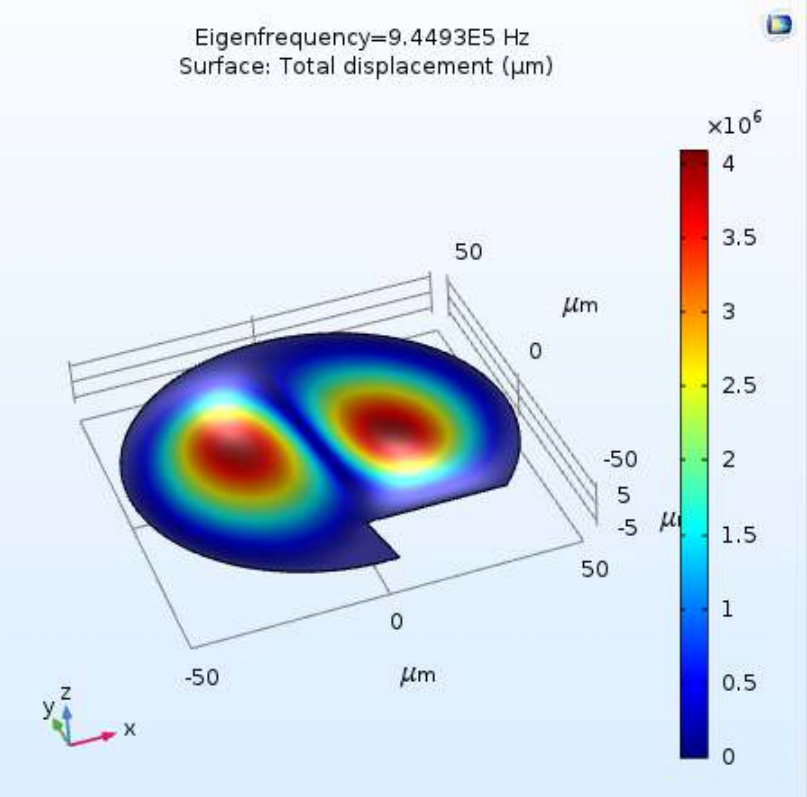

Figure 5.19: Mode shape and eigenfrequency of the second vibrational mode of B1A4 membrane

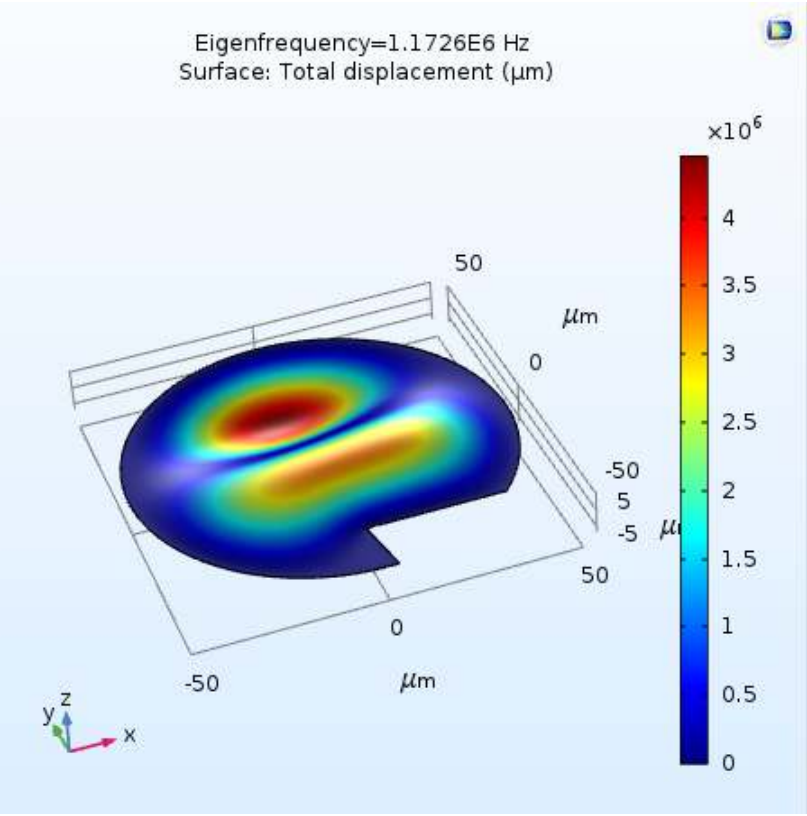

Figure 5.20: Mode shape and eigenfrequency of the third vibrational mode of B1A4 membrane

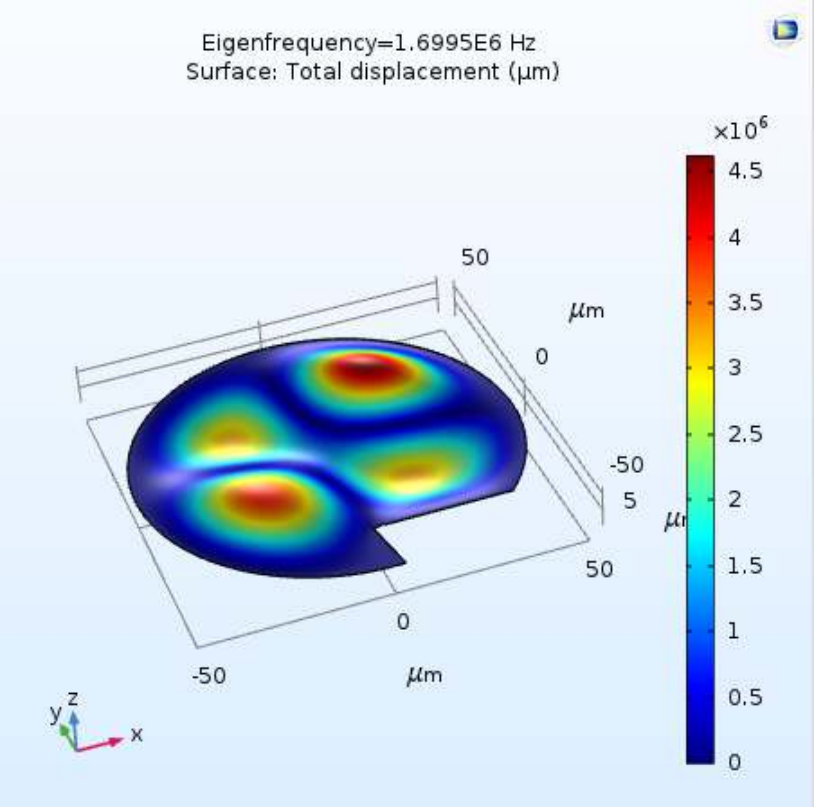

Figure 5.21: Mode shape and eigenfrequency of the fourth vibrational mode of B1A4 membrane

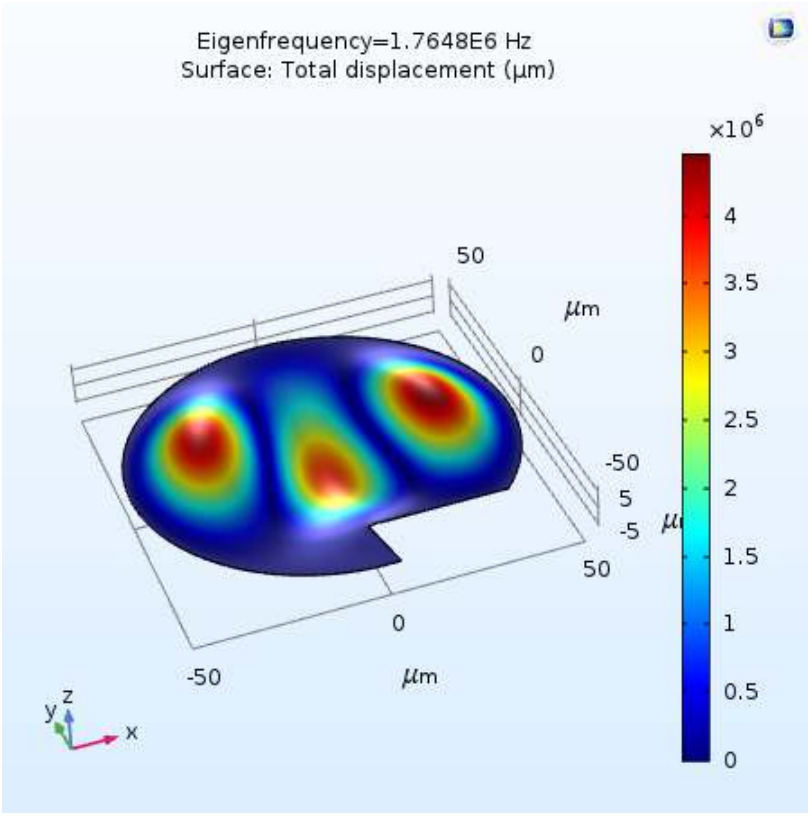

Figure 5.22: Mode shape and eigenfrequency of the fifth vibrational mode of B1A4 membrane

The splitting of the modes will allow to immediately check the status and quality of the membrane. Therefore, the number of splitted modes seems to be proportional to the number of cracks or geometric defects which are present on it. As a result, the splitting of the modes makes it possible to check whether the membrane has defects or not, without using the Scanning electron microscope SEM or the Vibrometer in "White Light Mode".

Conclusions

As presented in the last chapter, the EPFL and G205n graphene drums samples are analyzed and they strictly reported similar behaviors. In both cases the trends of the respective first average frequency modes are proportional to 1/R, where R is the radius of the drum. The average tension value of the two sample is much similar, $\sigma_{EPFL} = 0.005$[N/m] for the EPFL sample and $\sigma_{G205n} = 0.003$[N/m] for the G205 one which was fabricated in Politecnico di Torino. The average Q factors value for both samples have the same order of magnitude, and it shows the same trend of decreasing with the diameter of the hole. This trend mainly depends on two factors, in fact the quality of the measurement (signal to noise ratio) obtained by using the Vibrometer worsening as the diameter of the drum decreases, in addition the quality of the Non Linear Lorenzian fit, performed with Origin software, is strongly dependent on the obtained measured signal, which results worst for circular membranes that have a short diameter, as already mentioned. Moreover, it has been verified that many of the graphene membranes under examination show the phenomenon of splitting the modes, that was also simulated by using Comsol software. This phenomenon can be exploited as a novel approach to determine the graphene membrane quality. In fact, while an intact membrane shows a frequency spectrum that follow the circular membrane theory, the phenomenon of splitting occurs on membranes where cracks and breakages are present. These defects break the symmetry of the membrane leading to the split of the degenerate modes. The samples that show the best results are those produced via Wet-transfer Dry-etching of the PMMA. This was determined with a detailed study of the various transfer processes of graphene over the substrate. Instead, the Wet transfer-Wet etching of the PMMA process and the Dry-transfer Wet-etching of the PMMA process gave the worst results. The breakthrough was linked to the Dry etching of the PMMA carried out by thermal removal by inserting the sample into a hot furnace. The samples treated with this approach showed a higher number of covered holes. Moreover, the quality of graphene is closely linked to the aging quality of the Copper where it is deposited, in fact the best graphene drum samples were produced with "fresh" graphene. From the results presented in this work, it is underlined how graphene represents a material with very interesting mechanical properties. Its low mass density leads to the possibility of fabricating nanomechanical resonating device showing high frequencies working ranges of the order of tens of MHz, paving the way to their application as a high sensitivity mass, force and pressure sensors.

Bibliography

[1] A. K. Geim and K. S. Novoselov "The rise of graphene",2007, Nat. Mater.

[2] A. K. Geim and K. S. Novoselov, “Electric field effect in atomically thin carbon films”, 2004, Science

[3] A. K. Geim and K. S. Novoselov,“The electronic properties of graphene”,2009,Rev. Mod. Phys.

[4] C. Lee and J. Hone,“Measurement of the elastic properties and intrinsic strength of monolayer graphene”,2008, Science

[5] Richard Feynman,“Plenty of Room at the Bottom”,2008

[6] Massimiliano Di Ventra, James E. Hughes Jr; Stephane Evoy, "Introduction to Nanoscale Science and Technology (Nanostructure Science and Technology)", Berlino, Springer, 2004

[7] J.Scott Bunch, Arend M.van der Zande, "Electromechanical Resonators from Graphene Sheets", 2007, Science

[8] Vergara-Cruz, A. Bachtold, "Force sensitivity of multilayer graphene optomechanical devices", 2016, Nature Comunications

[9] Abhinandan Borah, Mandar M Deshmukh, "Low tension graphene drums for electromechanical pressure sensing", 2015, 2D Materials

[10] Myung-Ho Bae and Yun Daniel Park, "Bright visible light emission from graphene", 2015, Nature nanotechnology

[11] Kenneth Shepard and James Hone, "Graphene mechanical oscillators with tunable frequency", 2013, Nature nanotechnology

[12] R. Vijay and Mandar M. Deshmukh, "Dynamical strong coupling and parametric amplification of mechanical modes of graphene drums", 2016, Nature nanotechnology

[13] KilhoEoma , HaroldS.Parkb, "Nanomechanical resonators and their applications in biological/chemical detection:Nanomechanics principles", 2011, Physics Reports

[14] Villanueva, Nanomechanic, 2013, Springer

[15] Ji Won Suk, and Rodney S. Ruoff, "Transfer of CVD-Grown Monolayer Graphene onto Arbitrary Substrates", 2011 , ACS Nano

[16] S. Kataria and M.C. Lemme, "Graphene method for the fabrication of membrane-based Nems", 2016, Elsevier

[17] Robert A. Barton , Jeevak Parpia, "Fabrication and performance of graphene nanoelectromechanical systems", 2011

[18] McMullan, D. "Scanning electron microscopy 1928–1965", 2006

[19] McMullan, D. "Von Ardenne and the scanning electron microscope", 1988

[20] Gardiner, D.J. Practical Raman spectroscopy. 1989. Springer-Verlag.

[21] Jimenez-Sandoval, "Micro-Raman spectroscopy: a powerful technique for materials research" , 2000, Elsevier

[22] Ado Jorio, Riichiro Saito, Gene Dresselhaus, and Mildred S. Dresselhaus, "Raman Spectroscopy in Graphene Related Systems"

[23] Sergey Mikhailov, "Physics and applications of graphene experiments"

[24] Toshiaki Enoki, "Physics and chemistry of graphene"

[25] Peter Hagedorn, Anirvan DasGupta, "Vibrations and Waves in Continuous Mechanical Systems"

[26] Satender Kataria and Max C. Lemme "Noninvasive Scanning Raman Spectroscopy and Tomography for Graphene Membrane Characterization", 2017, Nano Letters

[27] J. van der Zant, Peter G. Steeneken and Warner J. Venstra, "Visualising the motion of graphene drums", 2016, Nano Letters

[28] Asensio, Vignaud, "Towards high quality graphene growth and transfer", 2015, Elsevier

[29] A. H. Castro Neto, F. Guinea, and N. M. R. Peres, "Drawing conclusions from graphene", Physics World, 2006

[30] "Introduction to the Physical Properties of Graphene" Jean-No¨el FUCHS Mark Oliver GOERBIG Lecture Notes 2008

[31] "Engineers Prove Graphene is the Strongest Material",Columbia University , 2008

[32] "MSA-500 Micro System Analyzer Measuring 3-D Dynamics and Topography of MEMS and Microstructures" Polytec

[33] "JSM-7610F Schottky Field Emission Scanning Electron Microscope", Jeol

[34] "Scanning electron microscope", Encyclopaedia Britannica

[35] "Scanning Electron Microscopy (SEM)", HZDR, Thomas Heinig

[36] Kazuaki Sawada and Kazuhiro Takahashi. "Development of graphene drum resonator with nanocavity by low-pressure dry transfer technique", University of Technology, Toyohashi, Japan

[37] "CVD Graphene Growth/Transfer" , Ishigami Group Wiki Nanomaterial Research and More

[38] Nicholas Fantuzzi, Francesco Tornabene, Erasmo Viola, "Generalized Differential Quadrature Finite Element Method for Vibration Analysis of Arbitrarily Shaped Membranes", 2014